

Vision 20/20: Single photon counting x-ray detectors in medical imaging

Katsuyuki Taguchi^{a)}

Division of Medical Imaging Physics, The Russell H. Morgan Department of Radiology and Radiological Science, Johns Hopkins University School of Medicine, Baltimore, Maryland 21287

Jan S. Iwanczyk^{b)}

DxRay, Inc., Northridge, California 91324

(Received 27 March 2013; revised 15 August 2013; accepted for publication 16 August 2013; published 12 September 2013)

Photon counting detectors (PCDs) with energy discrimination capabilities have been developed for medical x-ray computed tomography (CT) and x-ray (XR) imaging. Using detection mechanisms that are completely different from the current energy integrating detectors and measuring the material information of the object to be imaged, these PCDs have the potential not only to improve the current CT and XR images, such as dose reduction, but also to open revolutionary novel applications such as molecular CT and XR imaging. The performance of PCDs is not flawless, however, and it seems extremely challenging to develop PCDs with close to ideal characteristics. In this paper, the authors offer our vision for the future of PCD-CT and PCD-XR with the review of the current status and the prediction of (1) detector technologies, (2) imaging technologies, (3) system technologies, and (4) potential clinical benefits with PCDs. © 2013 American Association of Physicists in Medicine. [<http://dx.doi.org/10.1118/1.4820371>]

Key words: photon counting, x-ray, computed tomography

1. INTRODUCTION

Since their discovery in 1895 by Wilhelm C. Röntgen, x-rays have been playing a critical role in medical imaging. They are helping radiologists and physicians to detect and characterize disease processes of the skeletal system, soft tissue, and their functionality. Transmitted and detected x-ray beams generate a snapshot projection image, a series of projection images, or cross-sectional tomographic images. X-ray (XR) systems provide two-dimensional images of the transmitted x-ray intensities. Multislice x-ray computed tomography (CT or multidetector-row CT) scanners provide three-dimensional images of the linear attenuation coefficient distribution within a patient, accurately delineating organs and tissues. However, there are four major limitations to current CT and XR technologies: (1) the contrast between different soft tissues is often insufficient; (2) images are not tissue-type specific (different tissue types can appear with similar pixel values); (3) “CT scanning is a relatively high-dose procedure;”¹ and (4) gray-scale pixel values of CT images, which should be linear attenuation coefficients, are not quantitative but qualitative (see Sec. 5.E for more discussion). These limitations result from or are made worse by the energy integrating detectors (EIDs) used in CT scanners and XR systems.

Factors influencing the x-ray linear attenuation coefficients include the chemical composition and mass density of the object, and the energy of the x-ray photons. Therefore, the transmitted x-ray spectra carry information about different tissue types (see Fig. 1). The EIDs, however, measure the energy-integrated signals of x-ray photons, thus losing all of the energy-dependent information. In addition, EIDs not only add electronic noise and Swank noise,² but also weight lower en-

ergy photons less, which carry larger contrast between tissues than higher energy photons. This results in increased noise and decreased contrast.

In general, dual-energy CT imaging³ can provide tissue-specific images. However, neither the current dual-kVp nor dual-source techniques⁴ provide optimal results, because there is cross-talk between the high and low energy images and the number of resolvable basis functions for material decomposition is limited to two (see Appendix A).³ A third basis function is required to identify contrast media containing elements with high atomic numbers. Thus, it is desirable to measure the transmitted x-ray photons in more than two energy windows.

Recently, photon counting detectors (PCDs) with energy discrimination capabilities based on pulse height analysis have been developed for medical x-ray imaging (see Fig. 2 and Table I).^{5–32} These PCDs count the number of photons of the transmitted x-ray spectrum using between two and eight energy windows. PCD-based CT and XR systems with multiple energy windows have the potential to improve the four major limitations we discussed before.^{6,7,33} Electronic and Swank noise affect the measured energy,³⁴ but do not change the output signal intensity (i.e., the counts), and the energy overlap in the spectral measurements can be smaller than that from any of the current dual-energy techniques using EIDs. In addition, more than one contrast medium can be imaged simultaneously and becomes distinguishable if the detectors have four or more energy thresholds or windows (see Fig. 1, right). PCDs may therefore lead to novel clinical applications as will be discussed in Sec. 5.

The performance of PCDs is not flawless, however, especially with the large count rates in current clinical CT. Due to the stochastic nature of time intervals between photon arrivals

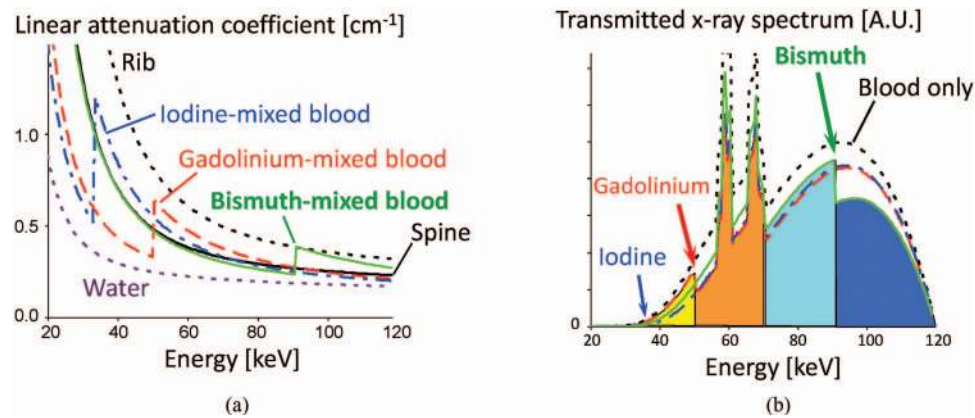


FIG. 1. (Left) Energy-dependent linear attenuation coefficients of various materials. Contrasts between different materials are larger at lower energies in general. Four materials, spine, 0.49% w/w iodine-mixed blood, 0.26% w/w gadolinium-mixed blood, and 0.28% w/w bismuth-mixed blood, would result in the same pixel value with the current EID-CT, although they have distinctly different attenuation curves. (Right) Transmitted spectra with 25 cm water and 5 cm blood without or with one of the three contrast agents. The K-edges of gadolinium and bismuth are clearly seen.

and the limited pulse resolving time, quasicoincident photons generate overlapping pulses which may be recorded as a single count with a wrong energy. This phenomenon is called pulse pileup and results both in a loss of counts, referred to as dead time loss, and a distortion of the recorded spectrum.³⁵ It is therefore critical to develop schemes to compensate for these effects. Other phenomena may also degrade the spectral response of PCDs, including incomplete charge collection generated by x-rays due to charge sharing and charge trapping

effects.^{31,36,37} We will review various performance degradation factors in Sec. 2.C.

Our aim with this paper is to provide the current status and future perspective of key technologies and applications of PCDs in medical imaging. We will direct our focus on CT imaging but most of the discussion is applicable to XR imaging as well. Three technologies discussed in Secs. 2–4 are the detector technologies, imaging technologies, and system technologies. Potential benefits and clinical applications of PCD-based CT and XR systems are discussed in Sec. 5, and Sec. 6 concludes the paper.

2. DETECTOR TECHNOLOGIES

We outline the detector architectures and detection mechanism for PCDs #1 through #6 in Table I in Sec. 2.A and other approaches for the other PCDs in Table I in Sec. 2.B. We will then explain various performance degradation factors in Sec. 2.C and present a design strategy on how to balance the conflicting effects using cardiac CT as an example. Note that PCDs are not flawless. The development of high-quality PCD-CT systems requires the other two technologies on imaging and system we will discuss in Secs. 3 and 4, respectively, which are specifically developed and optimized for the PCD used in the system.

2.A. Basic architectures and detection mechanism

We outline the basic architecture and detection mechanism of PCDs with pulse height analysis. Compound semiconductor sensors with a thickness of 2–3 mm are chosen for CT imaging to effectively absorb x rays in the 20–140 keV range. They are used to construct two-dimensional detector array with pixelated anodes, e.g., 16×16 pixels, with a pitch of 200–1000 μm . Sensors based on cadmium telluride (CdTe), cadmium zinc telluride (CZT), silicon (Si) are already in clinical use. However, there are very advanced research developments of sensors based on mercuric iodide (HgI_2) and gallium arsenide (GaAs). Given the technological improvements,

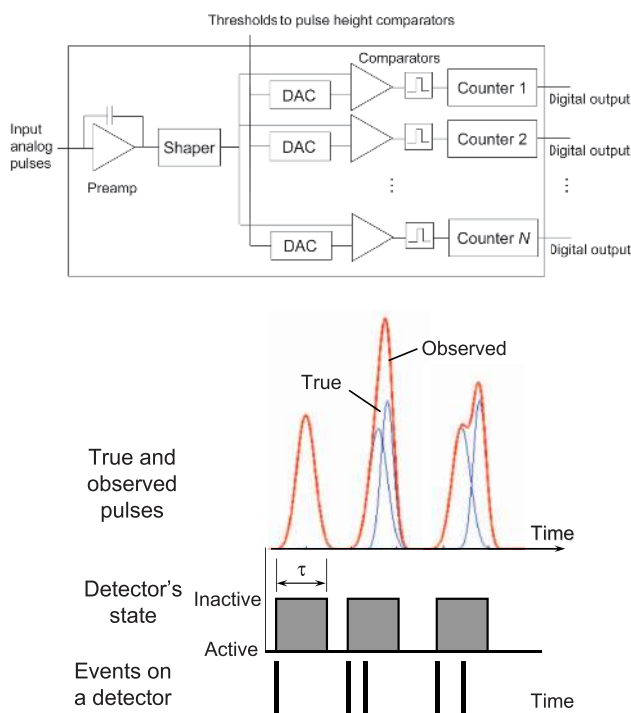


FIG. 2. (Top) The basic architecture of an individual channel with N energy thresholds in the ASIC. (Bottom) Each photon incident on a detector will generate a pulse whose height is associated with the photon energy. Quasicoincident photons within the detector deadtime τ are counted as 1 event with different energies from the originals due to pulse pileup effects. The former will result in lost counts and the latter in a distorted recorded energy spectrum.

TABLE I. Comparison of PCDs that have been or are being developed. This is not a complete list of all available PCDs but it provides a comprehensive review of different specifications. The detector systems listed in the table are not yet commercial products with the exception of the MicroDose Si slit detector that is introduced by Sectra and Philips for mammography applications. The other systems are in different stages of development representing at the time of writing. Most of them represent bench top experimental setups in research laboratories. DXMCT-1 detector arrays were used to fully populate a General Electric LightSpeed VCT scanner and prospective studies on patients were performed in a clinical environment (Ref. 5). It is not straightforward to compare the detector system parameters presented in this table, in particular because these detector systems were typically developed with a specific application in mind. For example, the Medipix development has a small pixel size and high spatial resolution and is better suited for imaging of small animals in preclinical applications than other detectors.

Index	Name/ASIC	Operation mode	Maximum count rates (Mcps/pixel)	Pixel size ($\mu\text{m} \times \mu\text{m}$)	Maximum count rates [Mcps/mm ²]	No. of energy thresholds per pixel	Tileup capability	Anti-charge sharing
1	DXMCT-1 (Refs. 5 and 8)		5.5	1000 \times 1000	5.5	2	2D	No
2	DXMCT-2 (Ref. 20)		5.5 ^a	500 \times 500	22 ^a	4	2D	No
3	Siemens 2010 (Refs. 17 and 28)		NA	225 \times 225	NA	2 or 4 ^b	NA ^c	No
4	ChromAIX (Ref. 16)		13.5 ^d	300 \times 300	150 ^d	4	1D	No
5	Hamamatsu (Refs. 10 and 11)		1-2	1000 \times 1000	1-2	5	1D	No
6	GMI CA3 (Refs. 6 and 9)		1-2	400 \times 1000	2-5	6	1D	No
7	Medipix3RX (Refs. 13, 29, and 52)	FM ^e -SPM ^f	0.21 ^g	55 \times 55	69.4 ^g	2	1D with 2 \times N (3-side butttable)	No
		FM ^e -CSM ^f	0.036 ^g	55 \times 55	11.9 ^g	1		Yes
		SM ^e -SPM ^f	0.145 ^h	110 \times 110	12 ^h	8		No
		SM ^e -CSM ^f	0.034 ^h	110 \times 110	2.8 ^h	4+4 ⁱ		Yes
8	CIX (Ref. 15)		3.3	250 \times 500	26	1	NA	No
9	Nexis Detector (Refs. 21 and 22)		2.0	1000 \times 1000	2.0	5	1D	No
10	MicroDose SI (Silicon strip) (Refs. 24–26)		0.056 ^j	50 \times 50	NA	2	1D	Yes ^k
11	KTH Silicon strip (Refs. 23, 27, and 30–32)		2.5 or 7.5 ^l	400 \times 500	200 or 600 ^m	8 ⁿ	2D ^o	No

Note: Maximum count rates are measured at full saturation unless otherwise specified.

^aMeasured at 15% deadline loss.

^bTwo per pixel, effectively up to four in chesspattern mode (Refs. 17 and 28).

^c2xN tiling must be possible, as 128 detector rows are formed by detector blocks with 64 \times 64 pixels (Ref. 17).

^dMeasured in electronics tests without detectors.

^eFine pitch mode (FM) and spectroscopic mode (SM).

^fSingle pixel mode (SPM) and charge summing mode (CSM).

^gMeasured with 300 μm thick silicon at 10% deadline loss.

^hMeasured with 2 mm thick CdTe at 10% deadline loss.

ⁱFour thresholds for summed charge, four for local charge.

^jMeasured at 10% deadline loss.

^kCoincident detection and store the counts to one of counters with no charge summing.

^lCount rates per layer with 16 layers per pixel. 2.5 Mcps/layer with 0.2% deadline loss, 7.5 Mcps/layer with 25% loss. The maximum output count rates not measured yet.

^mMeasured with 120 kVp. 200 = 2.5 \times 16/(0.4 \times 0.5) with 2% deadline loss and 600 = 7.5 \times 16/(0.4 \times 0.5) with 25% loss. The detection efficiency of 30 mm silicon is 80%.

ⁿEach detector pixel has 16 layers along the depth direction, and each layer has 8 energy thresholds. Energy information may also be available from depth of interaction, in which of the 16 layers the interaction took place.

^o<2% dead area after tiling (Ref. 47).

it may be possible in the near future to use polycrystalline films of the above materials for XR applications that offer a direct deposition technique onto CMOS or TFT readouts. The direct growth of x-ray converter materials onto the electronic readouts may be a very cost effective method to produce large area, high spatial resolution imaging arrays.^{38,39}

The individual pixelated anodes are connected to application-specific integrated circuits (ASICs) containing parallel channels. Each channel consists of an amplifier, a pulse shaper, N pulse height comparators for implementing adjustable energy windows, and N counters per detector pixel (see Fig. 2). The number of energy windows per pixel, N , varies among detector systems between two to six for PCDs #1 through #6 in Table I. A negative bias voltage with re-

spect to the anode is applied to a continuous metalized thin film cathode on the incident side of the CdTe sensor, creating an electric field along the depth direction of the sensor (note that the bias voltage is applied along the normal to the depth direction with a PCD with stacked layers which will be discussed in Sec. 2.B). The interconnections between detector arrays and silicon ASIC electronics are a very challenging task due to the large density of connections between dissimilar materials and different pitch and often different configuration of detector pixels and individual ASIC channels. Standard wire bonding or regular solder reflow technologies cannot be used with CZT or CdTe. Instead, low temperature solder reflow, silver epoxy, or other bump bonding technologies must be utilized. The assembly very often

involves interposer boards to assist the interconnections. The dense parallel channel method to increase throughput of a detection system is an approach utilizing an increased number of parallel detection and signal processing channels within a given area. However, densely packed multichannel fast electronics lead to large power consumption and the resulting heat needs to be dissipated to the ambience without negatively affecting the detection system. In order to reduce power consumption the shortest possible connections to the detector pixels for the lowest stray capacitance are considered.

PCDs count the number of photons within each of N energy windows as follows: When x-ray photons arrive at the PCD, the energy deposited by each x-ray photon incident onto the PCD generates electrical charges. The charges then travel within the detector under the influence of the electric field toward the electrodes and induce a pulse signal, which is then processed by the ASIC. The height of the pulse is compared with a given energy threshold value. A count is registered in the counter associated with the given comparator if the pulse height exceeds the threshold value. Subtracting counts in counters from adjacent energy threshold values yields the counts in the energy window defined by the two threshold values. Digital-to-analog-converters (DAC) allow for fine tuning of the threshold values for each channel as well as for compensating channel-to-channel offset variations through calibration procedures.

Note that “peaking time” and “deadtime” will be used in this paper when the speed of PCDs is discussed. The peaking time is the time required for a pulse shaped by amplification/processing electronics to reach its maximum amplitude, while the deadtime is the minimum amount of time that must separate two pulses in order for them to be recorded as two separate events. The deadtime is related to the peaking time, and the theoretical minimum deadtime is equal to two times the peaking time. However, the deadtime is much longer in practical detection system, where implementations particularly in ASIC electronics require simplest solutions due to a very large number of channels.^{40,41}

2.B. Other architectures and detection mechanism

2.B.1. Sensors

In order to develop photon-counting x-ray imaging detectors for CT, the high count rate combined with a need for high detection efficiency requires the development of detector structures that can provide formation of the response signal much faster than the transit time of carriers over the whole detector thickness. A number of strategies have been investigated for this purpose including the following detector structures: (a) detectors utilizing the “small pixel effect,”⁴² (b) parallel drift structures, (c) multiple stacked layers, and (d) a combinations of the above. There are merits and limitations inherent with each of these approaches.

2.B.1.a. Small pixel effect. The small pixel effect is achieved in detectors with pixel dimensions smaller than the detector thickness. The electrode configuration creating the small pixel effect is very effective in reducing the duration

of the fast portion of an induced signal because the induced signal is almost entirely due to the motion of the electrons as they approach the vicinity of the pixel anode. The pixel size, however, cannot be too small. When pixels are very small ($\ll 0.5$ mm) with a sensor thickness of 2–3 mm required for detection efficiency in CT, there are significant penalties to be paid in the form of energy spectral distortions due to charge sharing between pixels (discussed later).

2.B.1.b. Drift structures. Another strategy to shorten the signal duration is the implementation of parallel drift structures.⁴³ Drift structures allow for the collection of electrons from larger volumes on a small anode.^{44,45} A good energy spectral response is preserved with this method, and fast signal formation is achieved due to the small anode dimensions. However, drift structures require a larger number of electrodes and smaller anodes than a corresponding electrode configuration using the small pixel effect for the same detector size. More electrodes and smaller anode dimensions may increase the difficulties involved in electrically connecting the sensor to the ASICs.

2.B.1.c. Multiple stacked layers. An alternative detector configuration approach involves multiple stacked layers of segmented detectors with varying layer thicknesses.^{23,46} Having multiple layers along the depth direction significantly decreases the count rates each layer needs to handle. The thickness of the individual layers is optimized for count rate performance and to avoid saturation. Another potential merit is a possibility of estimating the energy using the depth of interaction.⁴⁶ This approach has a number of challenges related to the interconnections between the various layers and readout electronics. In order to keep the detector layers close together, connections to the readout electronics need to be elongated which might cause additional stray capacitances and vulnerability to cross talk, if not carefully designed. The increased stray capacitance is particularly harmful at high count rates, contributing to high electronic noise and/or high power requirements for readout electronics. Also, detectors with multiple layers may be more expensive to produce.

Nonetheless, silicon-based multilayer PCDs have been investigated for CT and the technology makes steady progresses.^{23,27,30–32,47–51} With 16 layers per pixel and 8 energy thresholds per layer, the PCDs have achieved high count rates (see Table I). The small atomic number of silicon is overcome by increasing the total thickness up to 30 mm in the depth direction. The total detection efficiency is then about 80%. Unlike compound semiconductors, silicon has fewer problems with quality, uniformity, and cost of production. The energy resolution seems adequate: The majority of interactions of photons with silicon is Compton scattering, not the photoelectric effect, due to low atomic number of silicon. However, simulations have shown that the detected spectrum after scattering maintains the original spectrum. Energies deposited with Compton scattering interactions may be below the lowest photon energy of the true x-ray spectrum, e.g., 30 keV, thus, they can be well separated from the primary spectrum and potentially spectra can be corrected. If they are discarded, a limited signal-to-noise ratio could be a potential challenge, because a small fraction of photons interact due

to the photoelectric effect and contributes to the good energy resolution. Most studies have been conducted using simulations and experiments with laser beams; and recent studies with 120 kVp x-ray showed promising results.³²

2.B.2. ASICs

The PCDs discussed in Sec. 2.A have dense parallel channels of amplification and processing electronics that provide a dedicated electronic channel for each detector pixel. There are a number of approaches being investigated to develop unique ASIC readout electronics including: (a) common digital electronics, (b) anti-charge sharing schemes, and (c) simultaneously counting photons and integrating their energies.

2.B.2.a. Common digital electronics. Detectors may have a pixel pitch smaller than the intrinsic spatial resolution requirement for decreasing count rates per detector pixel. In that case several detector pixels could use common electronics such as discriminators and counters to reduce power consumption.¹³

2.B.2.b. Anti-charge sharing scheme. Due to charge sharing and fluorescent x-ray escape, a photon may be counted by adjacent detector pixels at wrong energies especially when the pixel size is small (discussed later). Medipix3RX features a network of charge summing circuits that communicate between adjacent 2×2 pixels for detecting coincidences and reconstructing charges. The reconstructed charge will then be exclusively allocated to a pixel with the largest charge once it exceeds a set energy threshold.^{13,29} The recorded spectra had substantially decreased low energy tailing and distinct K-escape peaks.⁵² The spectrum measured with a pixel pitch as small as $55\text{-}\mu\text{m}$ with anti-charge sharing looks comparable to that measured by a $165\text{-}\mu\text{m}$ pitch pixel without anticharge sharing, which has a nine times larger pixel area. The smaller continuum tail of the recorded spectrum may provide significant advantages in material decomposition and K-edge imaging. The spatial sampling pitch remains as small as $55\text{-}\mu\text{m}$, thus, the spatial resolution of CT and XR images may be higher than images with $165\text{-}\mu\text{m}$ pitch pixel. This is an intriguing approach; however, there are challenges as well. Complicated coincidence electronics for allocating charges reduce the count rate capabilities and generate additional heat (see Table I).

2.B.2.c. Simultaneously counting photons and integrating their energies. Another approach to cope with the very large dynamic range of the incoming x-ray photon flux is to simultaneously count the photons and integrate their energies using unique electronics.¹⁵ The photon-counting information is useful at low count rates and the energy integrated information can be used at very high rates, thus preventing saturation of the system.⁵³

2.C. Performance degradation factors in PCDs

One might be tempted to think that PCDs can solve almost all of the hardware-oriented problems and output perfect data, and that the image reconstruction methods only need to handle Poisson noise and scatter. Unfortunately, this is not the

case. The measurements of PCDs may deviate from the truth due to numerous factors. In this section, we discuss the main physical effects when measuring x-ray photons with PCDs—pulse pileup, charge sharing, K-escape x-rays, Compton scattering, and others—and how they lead to various degradations in both recorded counts and energy spectra.

2.C.1. Pulse pileup

Pulse pileup is always present in photon counting detector systems and is a function of the count rate and detector deadtime. Detector systems with longer deadtimes exhibit this effect at lower count rates. Multiple pulses generated by quasicoincident photons may be piled up and observed as one pulse, resulting in a loss of counts and a wrong registered energy (Fig. 2). With count rates as high as those required for CT and XR medical imaging, two types of pulse pileup effects are observed: peak pileup and tail pileup. Coincidences during the initial part of a pulse are recorded as a single count at a higher energy than the original pulse's energies. This is called peak pulse pileup.³⁵ The loss of counts is called deadtime loss (see Fig. 3). The long tail of the pulse affects the recorded energy of subsequent events. For bipolar-shaped pulses, a peak overlapping the tail of a preceding pulse results in a lower recorded energy, and for unipolar-shaped pulses in a higher recorded energy. This is called tail pulse pileup.³⁵ Both peak pulse pileup and tail pulse pileup distort the recorded spectrum, and the amount of distortion depends strongly on the count rate.

2.C.2. Charge sharing

When an x-ray photon is absorbed in a PCD, a charge cloud is initially created in the detector. These charges

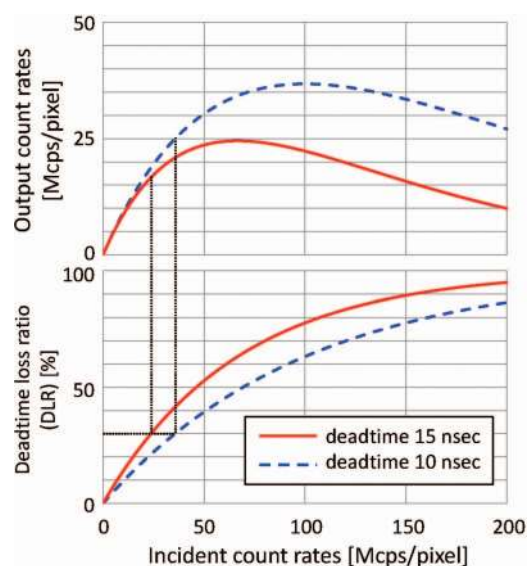


FIG. 3. Output count rates [million counts per second per detector pixel, Mcps/pixel] and DLR [%] of paralyzable detectors plotted over true count rates. For a peaking time of 5 ns or larger (see discussion in Sec. 2.D), the minimum deadtime is 10–15 ns. To limit the DLR up to 30% (see Sec. 2.D), the true count rates must be under 23.8 and 35.7 Mcps/pixel for 15 and 10 ns detector, respectively, which means that the theoretical maximum output count rates will be 16.6 and 25.0 Mcps/pixel, respectively.

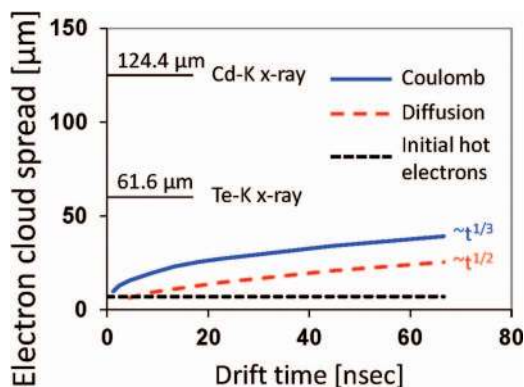


FIG. 4. Factors contributing to the spread of an electron cloud. Coulomb and diffusion contributions were calculated as a function of electron drift time assuming an electric field of $E = 3333$ V/cm and photon energy of 70 keV. It takes ~ 70 ns for an electron charge cloud to travel 3 mm in a CdTe layer. For reference, the mean absorption ranges of Cd-K and Te-K x-rays (discussed in Secs. 2.C.3 and 2.D) are 124.4 and 61.6 μm , respectively. Characteristic K x-rays ranges are calculated for the averaged energies of K-alpha 1 and K-alpha 2 because they are most prevalent. However, K x-rays ranges for K-betas are slightly longer because their energies are higher. Interest readers should consult Ref. 54 for more discussion. More analysis on the electron cloud spread due to Coulomb force and diffusion can be found, e.g., in Refs. 55 and 56, respectively.

(electrons and holes) drift to their respective electrodes due to the electric field generated by the applied high voltage bias. The charge cloud grows in size due to diffusion effects and the Coulomb force (Fig. 4). If the electron charge cloud reaches the anode near a pixel boundary, it may be divided and detected by multiple pixels at energies lower than the original energy, causing distortions in the spectral response (Fig. 5). The significance of this effect depends on the sensor material which governs the mobility of the charge carriers, the pixel sizes, the applied bias voltage, and the depth of interaction in the sensor.⁵⁷

2.C.3. K-escape x-rays

When an x-ray photon interacts with the PCD through the photoelectric effect, an electron in one of the inner shells of

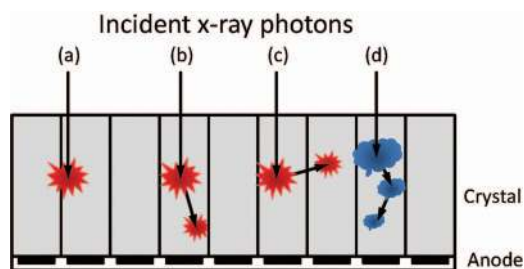


FIG. 5. Various interactions between incident x-ray photons and PCDs. (a) An interaction near pixel boundaries will be detected by multiple adjacent pixels (charge sharing). (b) The photoelectric effect results in a K-escape characteristic x-ray of the PCD sensor material, which is absorbed by the same pixel and results in quasicoincident events. (c) A K-escape x-ray is absorbed by another pixel, resulting in a loss of energy. (d) Multiple Compton scattering results in multiple quasicoincident events. A part of the signal may be detected by adjacent pixels.

the sensor atoms is ejected, leaving the atom ionized. The vacancy of the ejected electron is then filled by an electron from a higher orbit, and the transition energy can be realized as emission of either a characteristic “secondary” fluorescent x-ray photon or an electron (Auger effect). The photoelectric interactions with the detector material are the prevailing type of events at the low x-ray energies that are used in CT applications, and the production of characteristic radiation is a dominant effect due to the high fluorescent yields of Cadmium (Cd) and Tellurium (Te). Because the photons are emitted in a random direction, they may either be absorbed by the PCD pixel with the primary interaction again, be detected by an adjacent pixel, or leave the PCD completely (see Fig. 5). In the second and third cases, the recorded energy is lower by the K-shell energy, as the characteristic x-ray photon “escapes” from the pixel. In the first case, the two charge clouds generated by the primary and secondary x-ray photons may result in quasicoincident events, which may be detected as two separate counts if the detector electronics is fast or as a single count similar to pulse pileup effects if not.

2.C.4. Compton scattering

When an x-ray photon is scattered by the PCD, it changes the direction, loses some of its energy, and deposits the lost energy at the interaction site. This is called Compton effect or Compton scatter (Fig. 5). The photon may be absorbed by the PCD pixel, detected by an adjacent pixel, or leave the PCD completely. Contrary to the discrete energy loss with K-escape x-rays, the energy loss with Compton scatter depends on the scattered angle, thus, is continuous, resulting in a long tail at low energies.

2.C.5. Charge trapping

The internal charge trapping process is one in which an electron or hole is captured by a trapping center and then, after a delay, is thermally re-emitted into the conduction or valence band. The trapping centers are usually related to impurities and lattice defects in semiconductors. The trapping effect deteriorates spectral responses by reducing amplitudes of pulses toward lower energies than the original and by creating low energy tailing in the spectral characteristics.

2.C.6. Polarization and long-term reliability

Polarization and long-term reliability of the CdTe and CZT detectors could be a very serious problem for detectors exposed to high intensity x-ray beams. The polarization under certain operation conditions may lead to a decrease in the output count rates and charge collection efficiency which are dependent on time or incoming flux intensity.^{58,59} The polarization phenomenon is due to the existence of deep trapping levels in the detector material and several models have been proposed to explain this complex effect.^{58,60,61}

However, with proper selection of the starting material, well-chosen surface preparation, contact deposition, and good surface passivation, these detectors can operate stably and

reliably for a very long time. This has already been proven in commercial applications such as energy dispersive bone mineral density measurements. Two systems, Lunar iDXA systems (GE Healthcare) and Stratos DR systems (DMS-APELEM) with detectors from DxRay, Inc. were already introduced into the medical market several years ago. Good performance of the CdTe and CZT detectors under very high x-ray fluxes has been reported. However, their long-term reliability in CT applications still needs to be proven.

2.C.7. Other effects

There are a number of other factors influencing the performance of PCD system including the operation of amplification and processing electronics. The electronics are typically constructed as a multichannel ASIC where each channel is connected to a corresponding detector pixel. The shape of the amplified pulses, noise performance, energy linearity, and baseline behavior as a function of count rate plays an important role in the overall system performance.

2.D. Target specifications and design and strategy

Some of the above discussed factors lead to conflicting optimal detector system specifications. Thus, they need to be carefully considered and optimally balanced when a detector system is designed. Notice that it is not our intention to claim that the following describes the best design. Rather, in this section, we wish to show how one may balance the tradeoff of conflicting effects using the PCD discussed in Sec. 2.A and cardiac CT as an example. Different architectures such as anticharge sharing and stacked detection layers will very likely result in different conclusions; even with the same detector, the final design specifications may also depend on the target applications.

2.D.1. Conditions

A simulation was performed using the XCAT-DRASIM software package,^{62,63} which “scans” the XCAT phantom⁶⁴ (Fig. 6) with a CT simulator (DRASIM; Siemens Healthcare). Count rates onto the detector were calculated using the

following settings. **Patient:** Adult male with 50th percentile body size (347 mm chest width and 228 mm chest depth),⁶⁵ supine position; slightly off-centered to the anterior direction. **Scan:** 120 kVp; tube current modulation, 667 mA for lateral direction and 200 mA for the anterior–posterior direction; aluminum bowtie filter with thicknesses of 5–30 mm; focus-to-center-distance, 600 mm; focus-to-detector-distance, 1100 mm; 1892 channels for field-of-view of Ø500 mm; 2560 projections per rotation.

The true count rates reaching the detectors were as large as 161 Mcps/mm² for x-rays that travel just outside the boundary of the patient (Fig. 6). But due to the attenuation of the chest, the true count rates of x-rays through the cardiac and pericardial regions are significantly smaller. The maximum and average count rates for rays through the heart are as small as 9 and 3 Mcps/mm², respectively, which is well within the capability of the current or next generation PCDs. The maximum and average true count rates for rays within 16 cm in diameter are 18 and 3.5 Mcps/mm², respectively.

2.D.2. Upper limit of the peaking time

In order to limit the pulse pileup, it is necessary to shorten the peaking time and the overall pulse duration formed by the electronic circuit. This sets the upper limit on the peaking time of the amplification electronics. We assume in this paper that the deadtime losses due to pulse pileups should be limited to less than 10% without compensation and 30% with compensation. The upper limit of the peaking time required to achieve no more than 10% and 30% of deadtime losses for various detector pixel sizes for the input count rates of 20 and 200 Mcps/mm² are calculated using the paralyzable detection model^{40,41} and are shown in Table II. Notice that these criteria depend on various factors, such as the detection schemes, scan conditions, clinical applications, imaging tasks, and should be studied using task-specific performance tests.

2.D.3. Lower limit of the peaking time

In order to detect the total signal generated in a photoelectric or Compton scattering event, while considering x-ray escape of the characteristic x-rays of cadmium and tellurium, it

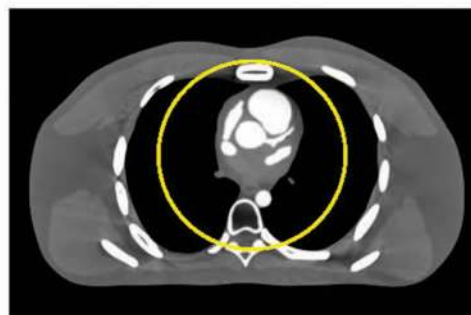
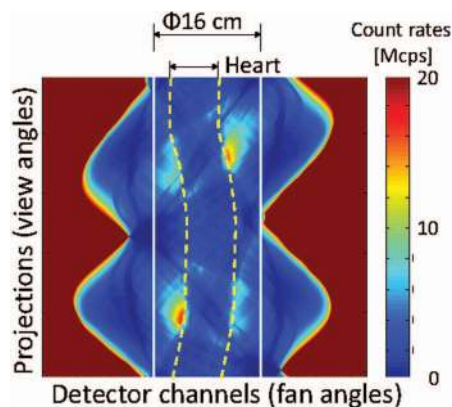


FIG. 6. (Left) Count rates of a typical cardiac CT scan shown in sinogram. (Right) XCAT phantom.

TABLE II. The required deadtime of the electronic circuit (ns) to limit the DLR less than 10% and 30%, respectively, for various true count rates and detector sizes.

Detector size (μm^2)	True count rates			
	20 (Mcps/ mm^2)		200 (Mcps/ mm^2)	
	DLR 10%	DLR 30%	DLR 10%	DLR 30%
1000×1000	5.3	17.8	0.5	1.8
750×750	9.4	31.7	0.9	3.2
500×500	21.1	71.3	2.1	7.1
250×250	84.3	285.3	8.4	28.5
50×50	2107.2	7133.5	210.7	713.3

is necessary to extend the peaking time of an electronic circuit to collect all of the ionization clouds generated by primary and secondary x-ray photons. This sets the lower limit on the minimum peaking time of the amplification electronics to collect the full charge to avoid spectral distortion. In order for an electron cloud to travel a distance that corresponds to the mean absorption ranges of Cd-K x-rays ($124.4 \mu\text{m}$), it takes 2.9 ns assuming typical electrical field in the detector. If the peaking time is just sufficient to collect the charge of the primary electron cloud with a size of $\sim 100 \mu\text{m}$, which is as short as 2.3 ns, it will not be able to collect the total signal generated by secondary x-ray photons with photoelectric and Compton scattering events from a single photon. Thus, it is necessary to extend the peaking time of the processing electronics no less than 5 ns.

2.D.4. Upper limit of the pixel size

Two influential factors are the target spatial resolution of reconstructed images and pulse pileups. The former sets the upper limit to the size of the current energy-integrating detectors, e.g., $1000 \mu\text{m}$. The upper limit of the pixel size is also set by the deadtime of the PCD and the expected maximum true count rates. If a PCD with a deadtime of 30 ns needs to handle a true count rate of up to 20 or 200 Mcps/ mm^2 with 30% deadtime loss ratio (DLR), the upper limit of the pixel size is 750 and $250 \mu\text{m}$, respectively (see Table II).

2.D.5. Lower limit of the pixel size

Unlike energy-integrating detectors, electronic noise of PCDs does not affect the recorded total counts, thus, it is not an influential factor. Three main factors to consider are K-escape x-rays, charge sharing, and Compton scattering. These effects will distort the recorded spectra, especially for small pixels. Thus, the lower limit of the pixel size must be sufficiently larger than the charge cloud size (Fig. 4) and the travel distance of K fluorescent photons as discussed below.³¹

The K fluorescent yield is the number of photons of all lines in the K series emitted in a unit time divided by the number of K-shell vacancies formed during the same time. The fluorescence yields of the K shells in Cd and Te are 84% and 87.5%, respectively.⁶⁶ This means that the photoelectric

interactions with a CdTe or CZT detector produce predominantly long range characteristic radiation rather than shorter range and highly absorbed Auger electrons. The mean range of the characteristic radiation can be expressed as the inverse of the linear attenuation coefficient. These values correspond to $124.4 \mu\text{m}$ for Cd-K x rays at 23.1 keV and $61.6 \mu\text{m}$ for Te-K x rays at 27.4 keV. The K-shell energy of zinc is 8.6 keV, thus, will be absorbed in a short distance. In addition, all the charge clouds generated by such secondary photons are subject to charge sharing at each location, resulting in a multiplicative effect (see Fig. 4). Our analysis showed that, at the absence of anti-charge sharing circuits, the above discussed effects set the lower limit of the pixel size to about $500 \mu\text{m}$ in order to preserve reasonably good spectral characteristics. Figure 16 of Ref. 5 shows a spectrum of Co-57 taken with 0.3 mm pixels and Fig. 9 of Ref. 67 was taken with 0.5 mm pixel. The spectrum distortions due to tailing are much smaller with 0.5 mm pixels.

Note that the lower limit can be smaller with an anti-charge sharing circuit. The effective pixel size is $N \times X \mu\text{m}$ with a physical detector pixel size of $X \mu\text{m}$ and the $N \times N$ pixel coverage of the circuit and the effective pixel size must be compared to the lower limit.

2.D.6. An example of comprehensive discussion

If the minimum peaking time is 5 ns, the deadtime will be 15 ns for a practical electronic circuit. If deadtime loss of up to 30% is acceptable, the maximum true count rates per detector pixel must be 23.8 Mcps/pixel and the maximum output count rates will be 16.6 Mcps/pixel with paralyzable detection model. If the lower limit of the pixel size is $500 \times 500 \mu\text{m}$, the maximum values of the true and output count rates per area will be 95.2 and 66.4 Mcps/ mm^2 , respectively (see Fig. 3).

3. IMAGING TECHNOLOGIES

We outline the overall strategies and the current status and perspective of imaging technologies necessary to enable PCD-CT systems and PCD-XR systems.

3.A. Overall strategy

As discussed in Sec. 2.C, the performance of PCDs can be degraded due to the limited speed of the detector system and various physical effects. Ignoring a large bias (e.g., larger than 5% or 10%) in critical properties would result in a significant bias in reconstructed images. While PCDs will continue to improve, they can never be perfect. As discussed above, optimizing the performance of one aspect of the PCD may lead to worse performance in other aspects. For example, the unattenuated x-ray flux reaching the detector of clinical CT systems with no bowtie filter could be as large as $10^9 \text{ cps}/\text{mm}^2$ at 1 m from the x-ray focal spot. The effective deadtime of PCDs with 1 mm^2 must be smaller than 50 ps to limit the count rate loss to less than 5%. A small pixel size would improve the effective deadtime but the spectra would be degraded due to

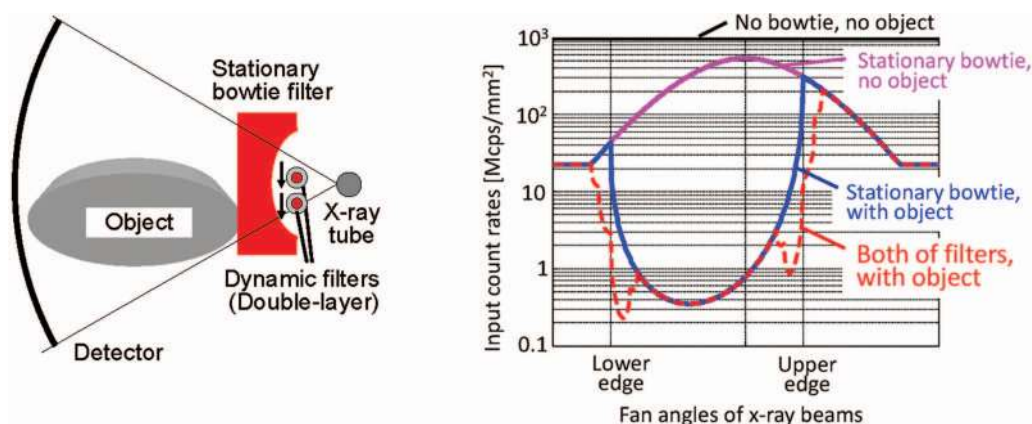


FIG. 7. Calculated true count rates in the lateral view of an elliptic water phantom when it is off-centered by 5 cm. Dynamic and stationary bowtie filters (left) decrease the count rates near the edges of the object (right, red curve), compared to the results without the dynamic filters (blue curve).

the charge sharing, K-escape x-ray, and Compton scattering especially without anti-charge sharing schemes.

Therefore, it is desirable to develop imaging technologies to overcome the limitations of PCDs. We believe that it is necessary to advance and integrate imaging methods in the following four areas for PCD-CT and PCD-XR systems in addition to the detector technologies discussed in Sec. 2:

- (1) X-ray beam-shaping filters to optimize the intensity and spectrum of x-rays;
- (2) calibration and compensation methods for the degradation effects of PCDs;
- (3) models of the PCDs degradation effects;
- (4) image reconstruction to provide accurate images from PCD data.

3.B. X-ray beam-shaping filters

New x-ray beam-shaping filters are desirable, which may consist of two components, a stationary part and a dynamic part, or a dynamic part only. With the two-component design, the stationary part “shapes” the intensity and spectrum of the x-ray beam across the field of view in general, while the dynamic part specifically shapes the x-ray beam near the edge of the imaging object.

The stationary part is similar to a conventional attenuating filter used in XR and CT systems. This is often referred to as a bow-tie filter for CT because it is thick at each end and thin in the middle; it is usually flat for XR. The purpose of the shaping filter is to equalize the x-ray intensity to the detector and to reduce or eliminate dose to the patient periphery. It is essential to manage the intensity near or outside the edges of objects for PCDs, as the unattenuated x-ray flux would be very intense otherwise. Further, for PCDs, the spectrum incident on the object needs to be shaped to maximize the spectral information acquired from the object.

The dynamic part would be a new component. A single stationary filter alone would not be sufficient, because the fan-angles in projections that correspond to the object’s edge change as the gantry rotates around the object. Additional filtrations or collimations, which dynamically track the edge

for each projection will be required. The maximum count rate requirement for the PCD could then be reduced significantly, e.g., from 10^9 cps/mm² for the unattenuated x-ray beam with 120 kVp to 10^8 cps/mm² after for the x-ray beam exiting the stationary bowtie filter, then further down to 10^5 – 10^8 cps/mm² with a dynamic bowtie filter and the object (Fig. 7).

Dynamic filters without a stationary component have already been investigated. One design split the stationary bowtie filter into two parts in the middle of the fan beam and each part independently moves along the fan angles to adjust the intensity of x-ray beams. Another design has a set of triangular wedges and each wedge independently moves longitudinally.⁶⁸ A third design has a hollow ellipse which rotates in the direction opposite to the gantry rotation.⁶⁹

3.C. Calibration and compensation methods

There are two philosophically different approaches to deal with distorted spectral data: corrections and compensation. Corrections attempt to undo the distortion process, while compensation is to offset the effect. Suppose that a forward imaging process to obtain an ideal x-ray spectrum y through an entire object x can be expressed as $h: y = h(x)$. The spectrum y is then skewed to y' by PCD degradation factors g , i.e., $y' = g(y)$, which is then recorded as counts within N energy windows, i.e., $z = f(y')$. Note that the spectra y and y' can be described reasonably well by counts within narrow energy windows, e.g., 1 keV.

The process of corrections is to estimate y from z ,⁷⁰ then reconstruct x from y . The problem of this approach for PCD degradation factors is that the first step is ill-posed, because the number of energy windows is between two and eight and is much smaller than the number of parameters to fully describe the spectrum y , e.g., 200 windows for an energy range up to 200 keV, and different spectra y may produce the same set of counts, z . Nonetheless, a few approaches have been proposed.^{71,72} They work well if and only if assumptions implicitly used as constraints, e.g., the object consists only of water, are correct.

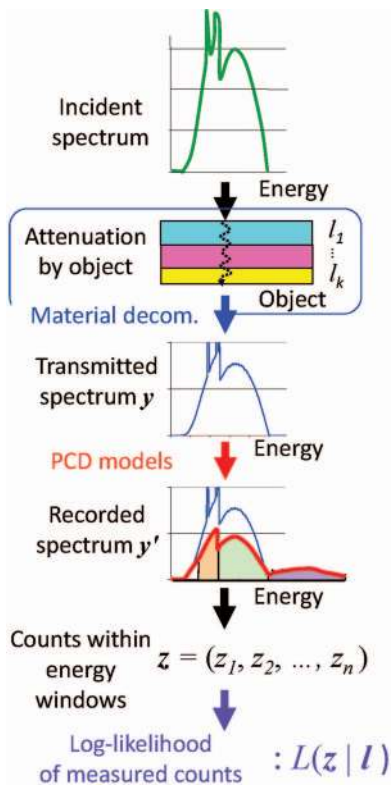


FIG. 8. The model of forward imaging process used in maximum likelihood methods to compensate for various spectral degradation factors.

The process of compensation is to estimate \mathbf{x} from \mathbf{z} by iteratively solving the forward process $\mathbf{z} = f(g(h(\mathbf{x})))$. Compensation of PCD degradation factors can be achieved by incorporating a PCD model as part of the forward imaging process, and iteratively estimating either the imaged object or the line integrals using a maximum likelihood approach.^{6,73–75} This can be formed as a well-posed problem, and the method is depicted in Fig. 8.

Step 1. The x-ray spectrum exiting from the bowtie (thus, incident onto the patient) and parameters necessary for the PCD model will be obtained during prescan calibrations. The patient is then scanned and counts are recorded in multiple energy windows, \mathbf{z} , for each ray. Variations of the true count rate and the spectrum of x-rays for each projection will be monitored as with current scanners.

Step 2. Using material decomposition techniques (see Appendix A and the blue frame and arrow in Fig. 8), we model the attenuation inside the object, \mathbf{x} , by the thicknesses of basis functions, $\mathbf{I} = \int \mathbf{x} dr$, through which the true transmitted spectrum and the input count rate can be calculated as $\mathbf{y} = h(\mathbf{I})$.

Step 3. Using the PCD models, the ensemble mean of the recorded, distorted spectrum are calculated as $\mathbf{y}' = g(\mathbf{y})$ (red arrow).

Step 4. From \mathbf{y}' , the ensemble mean of counts in multiple energy windows can be calculated as $\mathbf{z} = f(\mathbf{y}')$ (black arrow).

Step 5. Finally, the likelihood of the measured data, $L(\mathbf{z} | \mathbf{I})$, can be calculated (purple arrow).

Note that the only unknowns for each ray are \mathbf{I} , i.e., the effective thicknesses or the line integrals of the basis func-

tions, which can be estimated by iteratively maximizing the (log-)likelihood function. Thus, this process compensates for the PCD degradation factors accurately, as long as the PCD models g is accurate.

Note also that the attenuation model in Step 2 is exact if k is equal to or larger than the sum of the number of physics phenomena and the number of heavy elements inside the patient. It is exact regardless of the number of biological tissue types, e.g., muscle, fat, blood, skin, ligament, tendon, bone. Two predominant physics phenomena, Compton (or incoherent) scattering and the photoelectric absorption, are sufficient to model the x-ray interactions with materials within the energy range of diagnostic x-ray. Rayleigh (or coherent) scattering typically accounts for less than 5% of the diagnostic x-ray spectrum range and occurs only in low energies. Pair production requires a photon energy of at least 1.02 MeV and plays no role in diagnostic imaging. Heavy elements include those used as contrast agents (e.g., iodine, gadolinium, or bismuth) and in medical devices, such as implants, stents, and bolts.

3.D. PCD models

The key to a successful PCD compensation is an accurate model of PCD degradation factors, g , used in Step 3. It is logically possible to perform PCD compensation successfully without any model. If the PCD is stable over a long period of time, one can acquire an extensive amount of calibration data to relate every possible \mathbf{x} to PCD data $\mathbf{z} = f(g(h(\mathbf{x})))$ with every possible combination of conditions, such as tube current, tube voltage, materials, and thicknesses of bowtie filters. This approach would not be practical, though, as the number of required calibration datasets is very large and PCD data may change at least a few percent over time. It may be more reasonable to take an approach which is similar to the one implemented with EID-CT systems: An extensive calibration procedure will be performed less frequently (e.g., semiannually); and a quick calibration procedure will be employed every day, from which parameters necessary for PCD models are estimated and used to monitor the temporal change of PCD data for quality control. Both the model and the extensive calibration data acquired previously will be used to generate pseudocalibration data, which would be acquired if an extensive procedure was performed.

The PCD degradation factors discussed in Sec. 2.C are either count rate-dependent or count rate-independent, and the integrated phenomenon can be modeled by cascading the corresponding models.^{76–78} Below we discuss models of both of these factors.

All of the count rate-independent phenomena can be integrated into a single spectral response function, which can be modeled based on measurements using radioisotopes or synchrotron radiation at very low count rate.⁷⁹ An example of a count rate-independent spectral response function is shown in Fig. 9. The stochastic nature of the count rate-independent spectral distortions leads to a probability distribution of the recorded energy E given the true photon energy E_0 , which can be described by a spectral response function $SRF(E, E_0)$.^{6,73} The function holds well as long as the properties of PCDs are

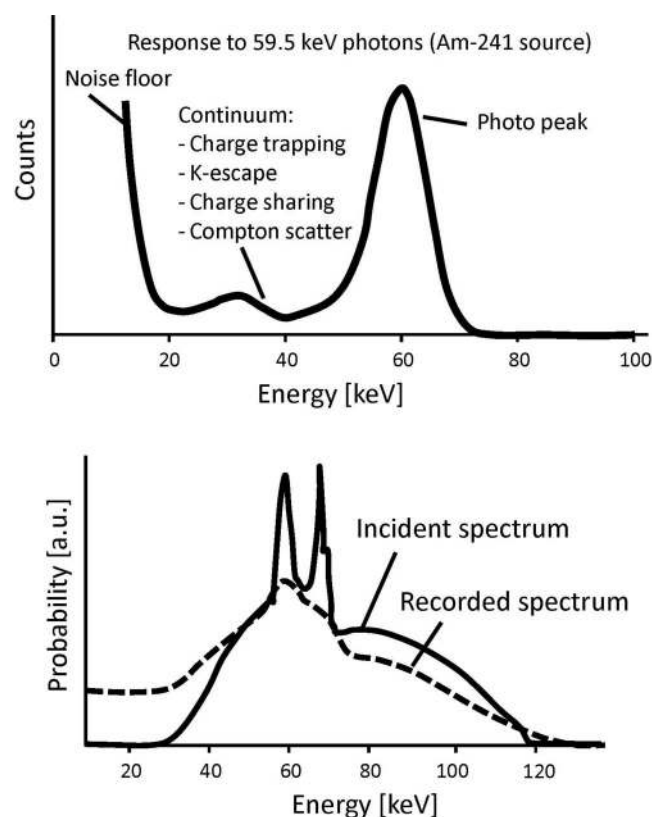


FIG. 9. (Top) An illustration of a typical spectrum recorded by a PCD using Am-241. The spectrum is distorted even at a very low count rate (i.e., the pulse pileup effects are minimal). (Bottom) There is a significant discrepancy between the true and recorded polychromatic x-ray spectra.

consistent over time. When a polychromatic x-ray spectrum $S(E_0)$ is incident onto the PCD, the recorded spectrum can be estimated by the integration of the $SRF(E, E_0)$ weighted by $S(E_0)$ over E_0 . Note that this process is not a convolution if $SRF(E, E_0)$ is a function of E_0 ; it is a convolution if the response is shift-invariant. An example of the true and recorded spectra is shown in Fig. 9. It can be seen that the count rate-independent spectral response of the PCD blurs the spectrum and increases counts especially at low energies.

The only count rate-dependent factor is pulse pileup. The spectrum distortion caused by pulse pileup is most difficult to model because it is a very complex phenomenon. But it is necessary to model, because the output depends on the input count rates and spectra, and thus, depends on the object to be imaged. Simple models, such as linear corrections or self-convolution,⁸⁰ are not accurate for modeling complex mechanisms of distortion. Various pulse pileup models have been developed,^{35,81–84} and we have developed a model^{83,84} that satisfies the accuracy, efficiency, and ability to handle a large number of coincidence requirements for high input count rates. The pulse pileup model accounts for the (bipolar) shape of the pulse, the distribution function of time intervals between random events, and the transmitted spectrum as the probability density function. The model showed excellent agreement with Monte Carlo simulation⁸³ and with PCD data (Fig. 10).⁸⁴ The coefficients of variation (i.e., the root mean square difference divided by the mean of measure-

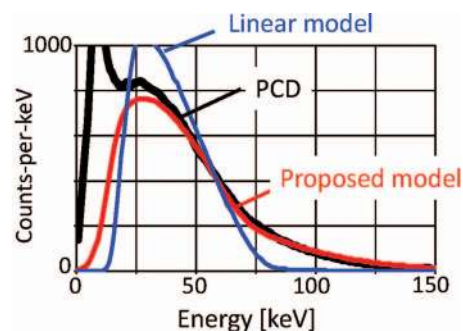


FIG. 10. The spectrum recorded by a PCD was severely distorted by pulse pileup effects and there is a significant discrepancy from the spectrum predicted by a linear model (i.e., the true spectrum linearly scaled by the dead-time loss ratio). In contrast, the PCD model proposed in Ref. 84 accurately estimated the recorded spectrum. The coefficient of variation was as small as 7.2%, while the deadtime loss ratio was as much as 46%. Reprinted with a modification from K. Taguchi, *et al.*, “Modeling the performance of a photon counting x-ray detector for CT: Energy response and pulse pileup effects,” *Med. Phys.* **38**, 1089–1102 (2011) (Ref. 84).

ments) were as small as 5.3%–10.0% for dead-time loss up to 50% in a Monte Carlo simulation⁸³ and 7.2% with deadtime loss of 46% in a PCD experiment.⁸⁴

3.E. Image reconstruction

The fourth area for advancing and integrating imaging methods is to adapt advanced image reconstruction methods for photon counting CT data for the interior problem and spectral data.

3.E.1. Interior problem

Even with the above-discussed PCD compensation schemes, photon counting data may be inaccurate especially for x-rays that go through the edge of the object or just outside the object when the object is off-centered. Reconstructing images from such inaccurate data will result in undesirable artifacts. From the algorithmic point of view, this is a unique, softly posed interior problem. The detector size defines the physical data truncation range. However, for acceptable data quality, only a subset of all detector channels may be used for reconstruction, for example, because the count rates were high in the periphery. The usable range depends on the PCD compensation method and can be decided retrospectively for PCD-CT. Insight into this unique problem can be gained by studying the tradeoff between acceptable data quality and image fidelity using simulation and phantom studies.

There are two approaches to address the interior problem: (i) to estimate unmeasured data and “detruncate” the projection data followed by a standard image reconstruction method; or (ii) to reconstruct (quasi-)exact images only from the truncated measured data. Studying these methods for the softly posed interior problem is certainly of interest.

For the first approach, various detruncation methods have been proposed, which include empirical approaches aiming to decrease an abrupt change between the estimated and measured data^{85,86} or more mathematically rigorous approaches

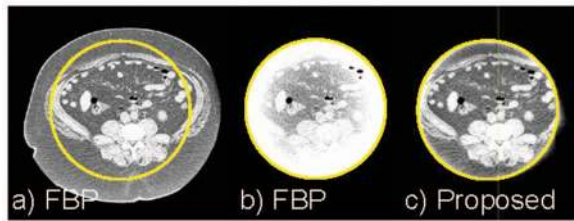


FIG. 11. Reconstructed images (a) without or (b) and (c) with truncation outside the circle, using (a) and (b) filtered backprojection or (c) the proposed sequential method. The image reconstructed by the proposed method showed very little bias throughout the region-of-interest except near the edge of the region-of-interest, while the image appeared very similar to that reconstructed without truncation. Reprinted with a modification from K. Taguchi, *et al.*, “Interior region-of-interest reconstruction using a small, nearly piecewise constant subregion,” *Med. Phys.* **38**, 1307–1312 (2011) (Ref. 96).

using the consistency conditions.^{87,88} The use of prior conventional CT images for photon counting data has been proposed lately.⁸⁹

Regarding the second approach, recently two important algorithms have been developed to solve the interior problem. First, when a small region located inside the region-of-interest is known, the region-of-interest image can be reconstructed exactly using a differentiated backprojection framework.^{90–93} Second, if the region-of-interest is piecewise constant, an exact image can be reconstructed using the total variation minimization algorithm without other *a priori* knowledge.^{94,95} Clinical CT data satisfy neither of the requirements; however, it was demonstrated that quasiexact region-of-interest images can be reconstructed even from noisy clinical CT projections by sequentially using filtered backprojection, total variation minimization, and differentiated backprojection (Fig. 11).⁹⁶ Pixel values of a tiny flat region obtained by total variation minimization were used as *a priori* information during differentiated backprojection.

3.E.2. Spectral data

Spectral data that become available with PCDs open a large room to investigate and develop new methods for improved contrast-to-noise ratio, material decomposition, and statistical reconstruction. A study⁹⁷ showed that weighting energy-window data by a factor of E^{-3} , where E is the effective energy of the window, improved the contrast-to-noise ratio of images (see Sec. 5.A for various study results), and other weighting schemes have also been investigated.^{98,99} An application of local highly constrained backprojection reconstruction (HYPR-LR) broke free from the tradeoff between the contrast and the noise of monoenergetic images.¹⁰⁰ Recorded counts may *not* be Poisson distributed due to pulse pileup.^{101–104} Thus, it is desirable to study the characteristics of the data and to develop new statistical algorithms to process data and reconstruct images. In addition, there are several representation schemes for PCD images, such as monoenergetic CT images, material-specific (e.g., iodine) density maps, effective atomic number maps, and electron density maps. Different types of images may be optimally ob-

tained by using different algorithms. Integrating three steps—material decomposition, image reconstruction, and final output calculation—into a single step may improve the accuracy or precision or both of images.

4. SYSTEM TECHNOLOGIES

4.A. PCD-CT systems

The literature reports on at least two prototype clinical PCD-CT scanners and two animal PCD-CT scanners. The image quality and performance of the scanners may need to improve further; however, the studies certainly showed promises of spectral CT imaging and demonstrated that the era of PCD-CT systems may be around the corner. There are also some table-top CT systems with clinical and animal CT geometries.¹⁰⁵

A LightSpeed VCT scanner (GE Healthcare; Waukesha, WI) equipped with DxRay’s first generation PCDs (DXMCT-1) was operated with x-ray tube voltage and current of 140 kVp and 40 mA. Details of the imaging technologies discussed in Sec. 3 have not been disclosed; however, the clinical images obtained by the scanner look superb despite the limited detector speed.⁵ A SOMATOM Definition AS scanner (Siemens Healthcare; Forchheim, Germany) equipped with a half-size PCD was operated at 120 kVp and 30 mA to scan a 20 cm water phantom. The true count rates incident onto the detectors in the experiment were 1–50 Mcps/mm². The contrast of iodine solution was enhanced by 17%, even though no corrections of PCD degradation factors were applied.^{17,28} Other research groups have also developed CT systems and reported promising performance such as improved contrast-to-noise ratio⁷ and high spatial resolution.¹⁰⁵

An animal PCD-CT (Philips Research; Hamburg, Germany) was developed and equipped with Gamma Medica-Idea’s PCDs.^{6,9} Phantom and animal images obtained by the scanner showed that multiple contrast agents (iodine and gadolinium,⁶ or iodine and gold¹⁰⁶) were simultaneously imaged, that metal artifacts from stents were reduced,⁹ that the characteristic effect of K-edges was imaged,⁹ and that targeted molecules (fibrin^{107,108} or macrophage¹⁰⁶) were successfully enhanced by nanoparticle contrast agents. Another system (MARS; University of Canterbury; Christchurch, New Zealand) equipped with Medipix-3 detectors developed by CERN, and the performance will be reported soon.

4.B. PCD-XR systems

Two bone mineral density measurement systems, Lunar iDXA systems (GE Healthcare) and Stratos DR systems (DMS-APELEM) equipped with PCDs from DxRay, Inc., are already on market for several years. An x-ray mammography PCD-XR system (MicroDose Mammography; Philips Healthcare; Solna, Sweden) which is equipped with an edge-on silicon array PCD has been introduced to the clinic. A multislit scanning technique used in the system seems to make the amount of scatter in the data negligible, resulting in superb images at a very low

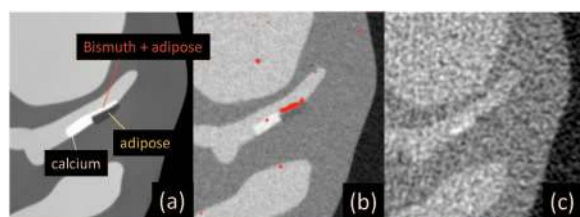


FIG. 12. (a) A computer simulated XCAT phantom image with bismuth at the surface of fatty atherosclerosis in a coronary artery (a). (b) and (c) Reconstructed images of the phantom scanned at the equivalent dose using a PCD-CT (b) and an EID-CT (c). Densities of bismuth are shown in red in (b). The PCD image has a better contrast-to-noise ratio and appears sharper than the EID image. This is also an example of K-edge, molecular, and simultaneous multiagent imaging. Reprinted with a modification from J. Cammin, *et al.*, "Spectral response compensation for photon counting clinical x-ray CT and application to coronary vulnerable plaque detection," *Proceedings of the Second International Meeting on Image Formation in X-Ray Computed Tomography*, edited by F. Noo (Salt Lake City, UT, 2012) pp. 186–189 (Ref. 113).

dose (<1 mGy). The performance of various PCDs has been tested in PCD-XR settings,^{10–12,109} which demonstrated advantages of PCDs such as low noise, high spatial resolution, K-edge imaging, energy-dependent attenuated x-ray images, and phase contrast-like enhanced edges in special settings.^{110–112}

5. POTENTIAL BENEFITS AND CLINICAL APPLICATIONS

We outline clinical merits and applications of PCD-CT and PCD-XR imaging systems, from improved and evolutionary versions of what is currently available (Sec. 5.A) to innovative and revolutionary ones (Sec. 5.H). We have performed a simulation study to demonstrate some of the merits discussed below in coronary CT angiography (Fig. 12). Scan conditions were as follows. 120 kVp; tube current modulation up to 667 mA for lateral direction, down to 200 mA for the AP direction; aluminum bowtie filter with thicknesses of 5–30 mm; focus-to-center, 600 mm; focus-to-detector, 1100 mm; 1892 channels for field-of-view of $\varnothing 500$ mm for PCD-CT; and 946 channels for EID-CT; 2560 projections per rotation. Images shown in Fig. 12 are reconstructed while compensating for the count rate-independent spectral distortion using a penalized maximum-likelihood approach⁷⁴ and filtered backprojection for PCD-CT and filtered backprojection for EID-CT.

5.A. Improved contrast-to-noise ratio and contrast of CT and XR images

The performance indices of CT will improve with PCDs and appropriate algorithms, and material decomposition allows to reconstruct monoenergetic images at desirable energies. Note that as shown in Ref. 114, results depended strongly on the condition under which the studies were conducted, such as the choice of object, the level of spectral distortion of PCDs, and the algorithms employed for compensation and image reconstruction. One simulation study showed that with optimal energy weighting, the contrast-to-noise ra-

tios of PCD-CT images were better than those of EID-CT images by 15%–57% depending on the materials.⁹⁸ When the effect of count rate-independent spectral distortion was incorporated, contrast-to-noise ratios of PCD-CT images were improved from EID-CT by 1.4%–11.6% in one study⁷³ and by 40%–63% in another study.⁷⁴ An experimental study using PCD-CT and clinical dual-energy CT, contrast-to-noise ratio of oil and water improved by 57%–96%.¹¹⁵ Another experimental study showed that the contrast-to-noise ratio of iodine solution against water increased by up to 20%.¹¹⁶ These improvements are significant for any applications, and particularly important for molecular imaging, since weaker signals can be detected.

5.B. Dose reductions of x-ray radiation and contrast agents

PCD-CT has the potential to improve the contrast-to-noise ratio of contrast-enhanced lesions at a given dose by, e.g., 30%. Either the amount of contrast agent or radiation dose can be reduced while maintaining the contrast-to-noise ratio of the lesion at the current level. Using the linear method shown in Appendix B, the contrast dose might be reduced by 23% or the radiation dose by 41%. Note that the amount of actual dose reduction achieved may be smaller than these values, as the PCD-CT system and image reconstruction methods may be nonlinear.

5.C. Improved spatial resolution of CT images

In order to combat high count rates required for clinical CT, the pixel size of PCDs will likely be smaller than that of EIDs: 0.2–0.5 mm for PCDs in contrast to 1.0–1.4 mm for EIDs (see Appendix C for EID pixel sizes). Thus, the intrinsic spatial resolution of PCD-CT images defined by the Nyquist frequency of the sampling condition will be superior to that of EID-CT images. Reconstructed images may become sharper and more accurate due to decreased partial volume effects from small structures, such as calcium plaques, although it will come with increased noise.

5.D. Beam hardening artifacts

CT vendors have developed beam hardening correction methods for water and bone.¹¹⁷ But beam hardening artifacts with contrast agents remain a problem for cardiac images.^{118,119} PCD-CT will address this problem, and improve images with soft plaque, calcium/bone, and contrast-enhanced lumen.

5.E. Quantitative CT and XR imaging

Current CT pixel values are not quantitative; they are measured in Hounsfield units, which are linearly related to the linear attenuation coefficients of x-rays at some energy. However, it is not clear which energy it is. The effective energies of the transmitted x-ray spectrum vary greatly during a scan, depending on factors such as fan/cone angles due to effect of bowtie filters, the attenuation of the object, projection angles.

The effective energy for an image pixel cannot be calculated; thus, an exact physical meaning of pixel values cannot be defined. CT images can be made quantitative using well-defined energies, which is possible with PCDs. The physical properties of each image pixel can be accurately modeled using the concept of material decomposition and reconstructed from PCD data. The concentration of contrast agents at regions-of-interest can then be quantified, which will benefit applications such as cardiac perfusion CT. One problem of current perfusion CT is that it is necessary to subtract a baseline image from target images at different phases to calculate the enhancement due to the injection of the contrast agent. Misregistration due to motion results in inaccurate time-density curves, and thus, inaccurate perfusion measurements, such as blood flow. The calculated enhancement is also ambiguous because, the pixel values of CT images are not quantitative. Measuring the concentrations of the contrast agent in target images without subtracting the baseline image, enabled by the quantitative PCD-based CT imaging methods, will improve the accuracy of perfusion CT and other applications.

5.F. Accurate K-edge imaging

Dual-energy CT provides only two measurements with different energies;³ however, it is desirable to have three or more measurements for K-edge imaging for contrast-enhanced CT exams^{9,33} and for corrections of various data quality degradation factors. A combination of the material decomposition and the third basis function for an atom used in the contrast agent-of-interest (e.g., iodine, gadolinium) will make it possible to quantify the spatial distribution of contrast agents on a pixel basis. This is called K-edge CT imaging, which will enable quantitative imaging and allow for perfusion CT without baseline image subtraction, thus, eliminates errors from misregistration and increased noise. Note that the third basis function, i.e., PCD-CT with more than two energy windows, is necessary to model the attenuation curves of contrast agents with high atomic numbers (e.g., iodine, gadolinium, gold, bismuth), because the curves are discontinuous due to their material-specific K-shell binding energies (Fig. 1).

5.G. Simultaneous multiagent imaging

Simultaneous multiagent imaging⁶ for different functionalities may become possible. A large biological variation among animals and patients makes it difficult to interpret measured quantities of agents. By injecting two agents simultaneously, one with target receptors and labeled by one element and the other without receptors and labeled by another element, and imaging both simultaneously, the agent without receptor can be used as a control.¹²⁰ This will solve the problems with the interpretation.

5.H. Molecular CT with nanoparticle contrast agents and personalized medicine

A new type of contrast agents may enable molecular CT imaging.^{121–123} Nanoparticles of various size and function are

labeled by atoms for CT imaging. Large particles with a particle size of a few hundred nanometers (blood pool contrast agents) (Refs. 124 and 125) stay in the system longer than 24 h because they are not filtered out by the kidneys and carry more receptors, both of which enhance target-specific therapy and imaging. For example, $\alpha_v\beta_3$ -targeted nanoparticles^{126–129} have been used to detect, characterize, and treat angiogenesis. Labeling particles for x-ray CT is achieved by attaching atoms with high atomic numbers (e.g., bismuth), which are preferable because signal-to-noise ratios are higher than iodine due to the following reasons: (1) they attenuate more photons with the same particle concentrations than those with lower numbers; and (2) there are more x-ray photons near the K-edges (see Fig. 1).

There are many challenges in this development including: toxicity, stability, and clearance for safety; uniformity of particle size for functionality; and particle concentration or uptake for functionality and signal detection. Nonetheless, nanomedicine research aligns well with NIH's goal of personalized medicine. PCD-CT will be ideal for these biomedical applications and will play a vital role in advancing nanomedicine research.

6. DISCUSSION AND SUMMARY

The rapid progress of detector technologies in the last decade has brought clinical PCD-CT and PCD-XR systems within our reach. PCDs will continue to improve. Imaging technologies can lower the specifications required for clinical systems, and PCDs will be able to achieve the goals in several years. We foresee that once the proof-of-concept of PCD imaging is completed in 3–5 years, there may be clinical prototype systems of PCD-CT and PCD-XR in hospitals in several years. The first wave of PCD-XR systems has appeared in mammography and spot imaging may follow, where a smaller detector size is acceptable. Bone mineral density measurement systems are already present on the market.

PCD-CT and PCD-XR imaging is not an evolution but a revolution. Not only does it improve the current CT and XR images but it also opens the doors to innovative and novel applications such as molecular CT. We believe that the clinical impact will be tremendous if CT or XR, which are usually the first screening imaging modality, can achieve molecular imaging in addition to regular imaging. Moreover, it may be more accurate and quantitative than other modalities.

Other technologies must be developed in parallel in order to take full advantage of PCD-CT and PCD-XR systems. First, we need image processing techniques and software for the novel applications and quantitative analyses methods discussed before. With current CT and XR systems, an image pixel contains only intensity information; but with PCD-CT and PCD-XR systems, a pixel contains much richer information such as an energy-dependent linear attenuation coefficient, densities of multiple basis functions, an effective atomic number, an electron density, and a tissue type. How to present such images is a challenge. Second, computer-aided detection and characterization methods will be desirable to handle and help to present such rich information efficiently. Third,

biological databases for normal ranges of each gender and age groups on the above listed information need to be established such that radiologists can judge whether or not a patient needs immediate attention. Fourth, education systems for radiologists and technicians will have to be updated for the novel type of information. Fifth, radiologists and medical physicists will need to work much more closely with biochemists. The nanoparticle contrast agents may become customized and optimized for a subgroup of patients. We may be able to optimize protocols and techniques of PCD-CT scans proactively, e.g., the choice of energy threshold values, for more targeted CT imaging with nanoparticle agents.

ACKNOWLEDGMENTS

The authors thank Dr. Taly Gilat-Schmidt, Dr. Thomas Koenig, Dr. Michael Campbell, Dr. Anthony Butler, Dr. Ewald Roessl, Dr. Christoph Herrmann, Dr. Erik Fredenberg, Dr. Steffen Kappler, Dr. Mats Danielsson, and Dr. Cheng Xu for providing information for Table I and Sec. 2.B. The authors appreciate technical help by Dr. George S. K. Fung and Dr. Karl Stierstorfer for the use of the XCAT-DRASIM software package. The authors are grateful to Medical Physics Journal for inviting us to write this paper and to the Associate Editor and Referees of the paper for their constructive suggestions and valuable guidance to improve the quality of the paper. The authors appreciate editorial help by Dr. Jochen Cammin and financial support by the National Institutes of Health Research Grant Nos. R44 EB012379, R44 EB008612, and R44 RR024101.

APPENDIX A: MATERIAL DECOMPOSITION

The attenuations of various materials in patients are material-specific and energy-dependent (see Fig. 1). But all materials can be modeled by a linear combination of three “basis functions” with different energy-dependency—e.g., (a) the continuous part of the photoelectric effect, Compton scattering contribution, and discontinuous K-edge contribution of the contrast agent-of-interest, or (b) mass attenuation coefficients of water, bone, and the contrast agent. This method is called material decomposition,^{3,130} and is sufficiently accurate within the diagnostic x-ray energy range. An accurate material decomposition process will make it possible to quantify the spatial distribution of basis functions on a pixel basis.

Using Kelcz’s constrained material decomposition method,¹³¹ a method called “three-material decomposition” was implemented. The name is seemingly misleading, because the method does not use three basis functions. Instead, it decomposes an unknown tissue into a combination of three known biological tissues such as fat, liver parenchyma, and iodine for abdomen from two basis functions and one constrain. Accurate K-edge imaging may become possible from dual-energy data as long as the constraint is true; however, it will not work well with materials other than those three biological tissues such as muscle or bone.

APPENDIX B: CALCULATION METHODS

Suppose methods A and B provide the contrast of C_A and C_B , respectively, and noise standard deviations of σ_A and σ_B , respectively, and method B provides $\alpha \times 100$ [%] better contrast-to-noise ratio than method A,

$$C_B/\sigma_B = (1 + \alpha) \times C_A/\sigma_A. \quad (B1)$$

1. Relative reduction of radiation dose $\beta \times 100$ [%] to achieve a comparable contrast-to-noise ratio of images

Suppose we perform two scans at different radiation dose levels and operate methods A and B as follows: (1) performing a scan with a radiation dose of R_A and operating method A; (2) performing a scan with a dose of R_A and operating method B; and (3) performing a scan with a dose of $(1-\beta) \times R_A$ and operating method B.

When the contrast of images is independent of the radiation doses, the contrast and noise of the three protocols are C_A and σ_A for (1), C_B and σ_B for (2), C_B and σ_{B3} for (3). If both protocols (1) and (3) provide the same contrast-to-noise ratio of images, we have

$$C_A/\sigma_A = C_B/\sigma_{B3}. \quad (B2)$$

Assuming that image noise is inversely proportional to the square root of the dose, from (2) and (3) we get

$$R_A \sigma_B^2 = (1 - \beta) R_A \sigma_{B3}^2. \quad (B3)$$

Using Eqs. (B1)–(B3), we get

$$\beta = 1 - 1/(1 + \alpha)^2. \quad (B4)$$

2. Relative reduction of contrast dose $\gamma \times 100$ [%] to achieve a comparable contrast-to-noise ratio of images

Suppose we perform two scans with different contrast dose levels and operate methods A and B as follows: (1) performing a scan with a contrast dose of D_A and operating method A; (2) performing a scan with a dose of D_A and operating method B; and (3) performing a scan with a dose of $(1-\gamma) \times D_A$ and operating method B.

When the contrast of images is proportional to the contrast dose (e.g., the amount of enhancement of iodine-water solution against water), the contrast and noise of the three protocols are C_A and σ_A for (1), C_B and σ_B for (2), $(1-\gamma) \times C_B$ and σ_B for (3). If both protocol (1) and protocol (3) provide the same contrast-to-noise ratio of images, we have

$$C_A/\sigma_A = (1 - \gamma) \times C_B/\sigma_B. \quad (B5)$$

Inserting Eq. (B5) into Eq. (B1), we get

$$\gamma = 1 - 1/(1 + \alpha). \quad (B6)$$

APPENDIX C: EID PIXEL SIZES

Suppose EIDs consisting of N_{ch} channels are used with a typical clinical equi-angular fan-beam CT geometry such

as: focus-to-center-distance, $R = 600$ mm; focus-to-detector distance, $R_d = 1100$ mm; field-of-view of $2r_0 = 500$ mm. The detector channel pitch can then be calculated by

$$\Delta_{ch} = \frac{\text{asin}(r_0/R)}{N_{ch}/2} \times R_d. \quad (C1)$$

Inserting the above values into Eq. (C1), we get $\Delta_{ch} = 1.06$ and 1.41 mm for $N_{ch} = 896$ and 672 , respectively, which is the range of number of channels used in existing EID-CT systems.

^{a)}Author to whom correspondence should be addressed. Electronic mail: ktaguchi@jhmi.edu; Telephone: 1-443-287-2974; Fax: 1-410-614-1060.

^{b)}Electronic mail: jan.iwanczyk@dxray.com

¹F. A. Mettler, Jr., P. W. Wiest, J. A. Locken, and C. A. Kelsey, "CT scanning: Patterns of use and dose," *J. Radiol. Prot.* **20**, 353–359 (2000).

²R. K. Swank, "Absorption and noise in x-ray phosphors," *J. Appl. Phys.* **44**, 4199–4203 (1973).

³R. E. Alvarez and A. Macovski, "Energy-selective reconstructions in x-ray computerised tomography," *Phys. Med. Biol.* **21**, 733–744 (1976).

⁴L. Yu, A. N. Primak, X. Liu, and C. H. McCollough, "Image quality optimization and evaluation of linearly mixed images in dual-source, dual-energy CT," *Med. Phys.* **36**, 1019–1024 (2009).

⁵J. S. Iwanczyk, E. Nygard, O. Meirav, J. Arenson, W. C. Barber, N. E. Hartsough, N. Malakhov, and J. C. Wessel, "Photon counting energy dispersive detector arrays for x-ray imaging," *IEEE Trans. Nucl. Sci.* **56**, 535–542 (2009).

⁶J. P. Schlomka, E. Roessl, R. Dorscheid, S. Dill, G. Martens, T. Istel, C. Baumer, C. Herrmann, R. Steadman, G. Zeitler, A. Livne, and R. Proksa, "Experimental feasibility of multi-energy photon-counting K-edge imaging in pre-clinical computed tomography," *Phys. Med. Biol.* **53**, 4031–4047 (2008).

⁷P. M. Shikhaliyev, "Energy-resolved computed tomography: First experimental results," *Phys. Med. Biol.* **53**, 5595–5613 (2008).

⁸W. C. Barber, E. Nygard, J. S. Iwanczyk, M. Zhang, E. C. Frey, B. M. W. Tsui, J. C. Wessel, N. Malakhov, G. Wawrzyniak, N. E. Hartsough, T. Gandhi, and K. Taguchi, "Characterization of a novel photon counting detector for clinical CT: Count rate, energy resolution, and noise performance," *Proc. SPIE* **7258**, 725824–725829 (2009).

⁹S. Feuerlein, E. Roessl, R. Proksa, G. Martens, O. Klass, M. Jeltsch, V. Rasche, H.-J. Brambs, M. H. K. Hoffmann, and J.-P. Schlomka, "Multi-energy photon-counting K-edge imaging: Potential for improved luminal depiction in vascular imaging," *Radiology* **249**, 1010–1016 (2008).

¹⁰Y. Tomita, Y. Shirayanagi, S. Matsui, T. Aoki, and Y. Hatanaka, "X-ray color scanner with multiple energy discrimination capability," *Proc. SPIE* **5922**, 59220A (2005).

¹¹Y. Tomita, Y. Shirayanagi, S. Matsui, M. Misawa, H. Takahashi, T. Aoki, and Y. Hatanaka, "X-ray color scanner with multiple energy differentiation capability," in *Proceedings of the IEEE Nuclear Science Symposium and Medical Imaging Conference* (IEEE, Roma, Italy, 2004), pp. 3733–3737.

¹²A. P. H. Butler, N. G. Anderson, R. Tipples, N. Cook, R. Watts, J. Meyer, A. J. Bell, T. R. Melzer, and P. H. Butler, "Bio-medical x-ray imaging with spectroscopic pixel detectors," *Nucl. Instrum. Methods Phys. Res. A* **591**, 141–146 (2008).

¹³R. Ballabriga, M. Campbell, E. H. M. Heijne, X. Llopart, and L. Tlustos, "The medipix3 prototype, a pixel readout chip working in single photon counting mode with improved spectrometric performance," *IEEE Trans. Nucl. Sci.* **54**, 1824–1829 (2007).

¹⁴M. Firsching, A. P. Butler, N. Scott, N. G. Anderson, T. Michel, and G. Anton, "Contrast agent recognition in small animal CT using the Medipix2 detector," *Nucl. Instrum. Methods Phys. Res. A* **607**, 179–182 (2009).

¹⁵E. Kraft, P. Fischer, M. Karagounis, M. Koch, H. Krueger, I. Peric, N. Wermes, C. Herrmann, A. Nascetti, M. Overdick, and W. Ruettgen, "Counting and integrating readout for direct conversion x-ray imaging: Concept, realization and first prototype measurements," *IEEE Trans. Nucl. Sci.* **54**, 383–390 (2007).

¹⁶R. Steadman, C. Herrmann, O. Mulhens, D. G. Maeding, J. Colley, T. Firlit, R. Luhta, M. Chappo, B. Harwood, and D. Kosty, "ChromAIX: A

high-rate energy-resolving photon-counting ASIC for spectral computed tomography," *Proc. SPIE* **7622**, 762220–762228 (2010).

¹⁷S. Kappler, F. Glasser, S. Janssen, E. Kraft, and M. Reinwand, "A research prototype system for quantum-counting clinical CT," in *Medical Imaging 2010: Physics of Medical Imaging* (SPIE, San Diego, CA, 2010), Vol. 7622, pp. 76221Z–6.

¹⁸W. C. Barber, A. Arodzero, N. Malakhov, M. Q. Damron, N. E. Hartsough, D. Moraes, P. Jarron, P. Weilhammer, E. Nygard, and J. S. Wanczyk, "Guard ring elimination in CdTe and CdZnTe detectors," in *Proceedings of the IEEE Nuclear Science Symposium and Medical Imaging Conference* (IEEE, San Diego, CA, 2006), pp. 2414–2416.

¹⁹J. S. Iwanczyk, E. Nygard, O. Meirav, J. Arenson, W. C. Barber, N. E. Hartsough, N. Malakhov, and J. C. Wessel, "Photon counting energy dispersive detector arrays for x-ray imaging," in *Proceedings of the IEEE Nuclear Science Symposium and Medical Imaging Conference* (IEEE, Honolulu, HI, 2007), pp. 2741–2748.

²⁰W. C. Barber, J. C. Wessel, E. Nygard, N. Malakhov, G. Wawrzyniak, N. E. Hartsough, T. Gandhi, A. Arodzero, M. Q. Damron, D. Moraes, P. Jarron, P. Weilhammer, and J. S. Wanczyk, "High flux x-ray imaging with CdZnTe arrays," *IEEE Nuclear Science Symposium and Medical Imaging Conference* (IEEE, Anaheim, CA, 2012).

²¹F. Rupcich and T. Gilat-Schmidt, "Experimental study of optimal energy weighting in energy-resolved CT using a CZT detector," *Proc. SPIE* **8668**, 86681X (2013).

²²V. B. Cajipe, R. F. Calderwood, M. Clajus, S. Hayakawa, R. Jayaraman, T. O. Tumer, B. Grattan, and O. Yossifor, "Multi-energy x-ray imaging with linear CZT pixel arrays and integrated electronics," *Nuclear Science Symposium Conference Record* (IEEE, Rome, Italy, 2004), Vol. 7, pp. 4548–4551.

²³C. Xu, M. Danielsson, S. Karlsson, C. Svensson, and H. Bornefalk, "Performance characterization of a silicon strip detector for spectral computed tomography utilizing a laser testing system," *Proc. SPIE* **7961**, 79610S (2011).

²⁴E. Fredenberg, M. Hemmendorff, B. Cederstrom, M. Aslund, and M. Danielsson, "Contrast-enhanced spectral mammography with a photon-counting detector," *Med. Phys.* **37**, 2017–2029 (2010).

²⁵E. Fredenberg, M. Lundqvist, B. Cederström, M. Åslund, and M. Danielsson, "Energy resolution of a photon-counting silicon strip detector," *Nucl. Instrum. Methods Phys. Res. A* **613**, 156–162 (2010).

²⁶M. Aslund, B. Cederstrom, M. Lundqvist, and M. Danielsson, "Physical characterization of a scanning photon counting digital mammography system based on Si-strip detectors," *Med. Phys.* **34**, 1918–1925 (2007).

²⁷C. Xu, M. Danielsson, S. Karlsson, C. Svensson, and H. Bornefalk, "Preliminary evaluation of a silicon strip detector for photon-counting spectral CT," *Nucl. Instrum. Methods Phys. Res. A* **677**, 45–51 (2012).

²⁸S. Kappler, T. Hannemann, E. Kraft, B. Kreisler, D. Niederloehner, K. Stierstorfer, and T. Flohr, "First results from a hybrid prototype CT scanner for exploring benefits of quantum-counting in clinical CT," *Proc. SPIE* **8313**, 83130X (2012).

²⁹E. N. Gimenez, R. Ballabriga, M. Campbell, I. Horswell, X. Llopart, J. Marchal, K. J. S. Sawhney, N. Tartoni, and D. Turecek, "Characterization of medipix3 with synchrotron radiation," *IEEE Trans. Nucl. Sci.* **58**, 323–332 (2011).

³⁰C. Xu, H. Chen, M. Persson, S. Karlsson, M. Danielsson, C. Svensson, and H. Bornefalk, "Energy resolution of a segmented silicon strip detector for photon-counting spectral CT," *Nucl. Instrum. Methods Phys. Res. A* **715**, 11–17 (2013).

³¹C. Xu, M. Danielsson, and H. Bornefalk, "Evaluation of energy loss and charge sharing in cadmium telluride detectors for photon-counting computed tomography," *IEEE Trans. Nucl. Sci.* **58**, 614–625 (2011).

³²C. Xu, M. Persson, C. Han, S. Karlsson, M. Danielsson, C. Svensson, and H. Bornefalk, "Evaluation of a second-generation ultra-fast energy-resolved ASIC for photon-counting spectral CT," *IEEE Trans. Nucl. Sci.* **60**, 437–445 (2013).

³³E. Roessl and R. Proksa, "K-edge imaging in x-ray computed tomography using multi-bin photon counting detectors," *Phys. Med. Biol.* **52**, 4679–4696 (2007).

³⁴J. Tanguay, H. K. Kim, and I. A. Cunningham, "The role of x-ray Swank factor in energy-resolving photon-counting imaging," *Med. Phys.* **37**, 6205–6211 (2010).

³⁵L. Wielopolski and R. P. Gardner, "Prediction of the pulse-height spectral distribution caused by the peak pile-up effect," *Nucl. Instrum. Methods Phys. Res.* **133**, 303–309 (1976).

- ³⁶P. Guerra, A. Santos, and D. G. Darambara, "Development of a simplified simulation model for performance characterization of a pixellated CdZnTe multimodality imaging system," *Phys. Med. Biol.* **53**, 1099–1113 (2008).
- ³⁷E. G. d'Aillon, M. C. Gentet, G. Montemont, J. Rustique, and L. Verger, "Simulation and experimental results on monolithic CdZnTe gamma-ray detectors," *IEEE Trans. Nucl. Sci.* **52**, 3096–3102 (2005).
- ³⁸G. Zentai, L. D. Partain, R. Pavlyuchkova, C. H. Proano, M. M. Schieber, and J. Thomas, "Dark current, sensitivity, and image lag comparison of mercuric iodide and lead iodide x-ray imagers," *Proc. SPIE* **5541**, 171–178 (2004).
- ³⁹N. E. Hartsough, J. S. Iwanczyk, E. Nygard, N. Malakhov, W. C. Barber, and T. Gandhi, "Polycrystalline mercuric iodide films on CMOS readout arrays," *IEEE Trans. Nucl. Sci.* **56**, 1810–1816 (2009).
- ⁴⁰G. F. Knoll, *Radiation Detection and Measurement*, 3rd ed. (Wiley, New York, 2000).
- ⁴¹*Instruction Manual TC 244 Amplifier* (Oxford Instruments, Inc., Oxon, England, 1992).
- ⁴²H. H. Barrett and K. Myers, *Foundations of Image Science*, 1st ed. (Wiley-Interscience, New York, NY, 2003).
- ⁴³J. S. Iwanczyk, B. E. Patt, and E. Nygard, U.S. patent 7,170,049 (28 December 2004).
- ⁴⁴J. S. Iwanczyk, B. E. Patt, J. Segal, J. Plummer, G. Vilkelis, B. Hedman, K. O. Hodgson, A. D. Cox, L. Rehn, and J. Metz, "Simulation and modelling of a new silicon x-ray drift detector design for synchrotron radiation applications," *Nucl. Instrum. Methods Phys. Res. A* **380**, 288–294 (1996).
- ⁴⁵B. E. Patt, J. S. Iwanczyk, G. Vilkelis, and Y. J. Wang, "New gamma-ray detector structures for electron only charge carrier collection utilizing high-Z compound semiconductors," *Nucl. Instrum. Methods Phys. Res. A* **380**, 276–281 (1996).
- ⁴⁶E. Beuville, R. Cahn, B. Cederstrom, M. Danielsson, A. Hall, B. Hasegawa, L. Luo, M. Lundqvist, D. Nygren, E. Oltman, and J. Walton, "High resolution x-ray imaging using a silicon strip detector," *IEEE Trans. Nucl. Sci.* **45**, 3059–3063 (1998).
- ⁴⁷H. Bornefalk and M. Danielsson, "Photon-counting spectral computed tomography using silicon strip detectors: A feasibility study," *Phys. Med. Biol.* **55**, 1999 (2010).
- ⁴⁸M. Yveborg, C. Xu, E. Fredenberg, and M. Danielsson, "Photon-counting CT with silicon detectors: Feasibility for pediatric imaging," *Proc. SPIE* **7258**, 725825 (2009).
- ⁴⁹H. Bornefalk, C. Xu, C. Svensson, and M. Danielsson, "Simulation study of an energy sensitive photon counting silicon strip detector for computed tomography: Identifying strengths and weaknesses and developing work-arounds," *Proc. SPIE* **7622**, 76223P (2010).
- ⁵⁰H. Bornefalk, C. Xu, C. Svensson, and M. Danielsson, "Design considerations to overcome cross talk in a photon counting silicon strip detector for computed tomography," *Nucl. Instrum. Methods Phys. Res. A* **621**, 371–378 (2010).
- ⁵¹M. Yveborg, M. Danielsson, and H. Bornefalk, "Performance evaluation of a sub-millimetre spectrally resolved CT system on high- and low-frequency imaging tasks: A simulation," *Phys. Med. Biol.* **57**, 2373–2391 (2012).
- ⁵²T. Koenig, E. Hamann, S. Procz, R. Ballabriga, A. Cecilia, M. Zuber, X. Llopert, M. Campbell, A. Fauler, T. Baumbach, and M. Fiederle, "Charge summing in spectroscopic x-ray detectors with high-Z sensors," *IEEE Trans. Nucl. Sci.* (submitted).
- ⁵³E. Roessl, C. Herrmann, E. Kraft, and R. Proksa, "A comparative study of a dual-energy-like imaging technique based on counting-integrating read-out," *Med. Phys.* **38**, 6416–6428 (2011).
- ⁵⁴J. Iwanczyk, W. M. Szymczyk, and M. Traczyk, "X-ray fluorescence escape peaks in gamma-ray spectra detected by CdTe detectors," *Nucl. Instrum. Methods Phys. Res.* **165**, 289–295 (1979).
- ⁵⁵J. D. Eskin, "Semiconductor gamma-ray detectors for nuclear medicine," Ph.D. dissertation (The University of Arizona, 1997).
- ⁵⁶S. M. Sze, *Physics of Semiconductor Devices*, 2nd ed. (Wiley, Hoboken, NJ, 1981).
- ⁵⁷M. E. Myronakis and D. G. Darambara, "Monte Carlo investigation of charge-transport effects on energy resolution and detection efficiency of pixelated CZT detectors for SPECT/PET applications," *Med. Phys.* **38**, 455–467 (2011).
- ⁵⁸P. Siffert, J. Berger, C. Scharager, A. Cornet, R. Stuck, R. O. Bell, H. B. Serreze, and F. V. Wald, "Polarization in cadmium telluride nuclear radiation detectors," *IEEE Trans. Nucl. Sci.* **23**, 159–170 (1976).
- ⁵⁹C. Szeles, S. A. Soldner, S. Vydrin, J. Graves, and D. S. Bale, "Ultra high flux 2-D CdZnTe monolithic detector arrays for x-ray imaging applications," *IEEE Trans. Nucl. Sci.* **54**, 1350–1358 (2007).
- ⁶⁰H. L. Malm and M. Martini, "Polarization phenomena in CdTe: Preliminary results," *J. Appl. Phys.* **51**, 2336–2340 (1973).
- ⁶¹R. O. Bell, G. Entine, and H. B. Serreze, "Time-dependent polarization of CdTe gamma-ray detectors," *Nucl. Instrum. Methods* **117**, 267–271 (1974).
- ⁶²G. S. K. Fung, K. Stierstorfer, W. P. Segars, K. Taguchi, T. G. Flohr, and B. M. W. Tsui, "XCAT/DRASIM: A realistic CT/human-model simulation package," *Proc. SPIE* **7961**, 79613D–79616D (2011).
- ⁶³G. S. K. Fung, K. Stierstorfer, K. Taguchi, W. P. Segars, T. G. Flohr, and B. M. W. Tsui, "A realistic CT/Human-Model simulation package," in *Proceedings of the Second International Meeting on Image Formation in X-Ray Computed Tomography*, Salt Lake City, UT, 2012, pp. 66–69.
- ⁶⁴W. P. Segars, M. Mahesh, T. J. Beck, E. C. Frey, and B. M. W. Tsui, "Realistic CT simulation using the 4D XCAT phantom," *Med. Phys.* **35**, 3800–3808 (2008).
- ⁶⁵O. Ergonomics, PeopleSize 2008: The size of customers to come (online database), 2008 (available URL: <http://www.openeng.com/psz/index.html>).
- ⁶⁶W. Bambynek, B. Crasemann, R. W. Fink, H. U. Freund, H. Mark, C. D. Swift, R. E. Price, and P. V. Rao, "X-ray fluorescence yields, auger, and Coster-Kronig transition probabilities," *Rev. Mod. Phys.* **44**, 716–813 (1972).
- ⁶⁷W. C. Barber, E. Nygard, J. C. Wessel, N. Malakhov, G. Wawrzyniak, N. E. Hartsough, T. Gandhi, and J. S. Iwanczyk, "Energy-resolved photon-counting x-ray imaging arrays for clinical K-edge CT," *Nuclear Science Symposium and Medical Imaging Conference (NSS/MIC)* (IEEE, Valencia, Spain, 2011), pp. 4441–4446.
- ⁶⁸S. S. Hsieh and N. J. Pelc, "The feasibility of a piecewise-linear dynamic bowtie filter," *Med. Phys.* **40**, 031910 (12pp.) (2013).
- ⁶⁹E. Roessl and R. Proksa, "Dynamic beam-shaper for high flux photon-counting computed tomography," in *Workshop on Medical Applications of Spectroscopic X-ray Detectors* (CERN, Geneva, Switzerland, 2013).
- ⁷⁰S. Miyajima, K. Imagawa, and M. Matsumoto, "CdZnTe detector in diagnostic x-ray spectroscopy," *Med. Phys.* **29**, 1421–1429 (2002).
- ⁷¹S. Kappler, S. Hoelzer, E. Kraft, K. Stierstorfer, and T. G. Flohr, "Quantum-counting CT in the regime of count-rate paralysis: Introduction of the pile-up trigger method," *Proc. SPIE* **7961**, 79610T (2011).
- ⁷²E. Kraft, F. Glasser, S. Kappler, D. Niederloehner, and P. Villard, "Experimental evaluation of the pile-up trigger method in a revised quantum-counting CT detector," *Proc. SPIE* **8313**, 83134A (2012).
- ⁷³E. Roessl, B. Brendel, K. Engel, J. Schlomka, A. Thran, and R. Proksa, "Sensitivity of photon-counting based K-edge imaging in x-ray computed tomography," *IEEE Trans. Med. Imaging* **30**, 1678–1690 (2011).
- ⁷⁴S. Srivastava, J. Cammin, G. S. K. Fung, B. M. W. Tsui, and K. Taguchi, "Spectral response compensation for photon-counting clinical x-ray CT using sinogram restoration," *Proc. SPIE* **8315**, 8315–8337 (2012).
- ⁷⁵S. Srivastava and K. Taguchi, "Sinogram restoration algorithm for photon counting clinical x-ray CT with pulse pileup compensation," in *Proceedings of the First International Meeting on Image Formation in X-Ray Computed Tomography*, Salt Lake City, UT, 2010, pp. 5–9.
- ⁷⁶J. Cammin, J. S. Iwanczyk, and K. Taguchi, "Spectral/photon-counting computed tomography," in *Emerging Imaging Technologies in Medicine*, edited by M. A. Anastasio and P. J. L. Riviere (Taylor & Francis, London, 2012), pp. 23–39.
- ⁷⁷J. Cammin, J. Xu, W. C. Barber, J. S. Iwanczyk, N. E. Hartsough, and K. Taguchi, "Modeling photon-counting detectors for x-ray CT: Spectral response and pulse pileup effects and evaluation using real data," *Proc. SPIE* **8668**, 86680R (2013).
- ⁷⁸J. Cammin, J. Xu, W. C. Barber, J. S. Iwanczyk, N. E. Hartsough, and K. Taguchi, "A cascaded model of spectral distortions due to spectral response effects and pulse pileup effects in a photon-counting x-ray detector for CT," *Med. Phys.* (submitted).
- ⁷⁹H. Ding and S. Molloy, "Image-based spectral distortion correction for photon-counting x-ray detectors," *Med. Phys.* **39**, 1864–1876 (2012).
- ⁸⁰R. Guenzler, V. Schuele, G. Seeliger, M. Weiser, K. Boeringer, S. Kalbitzer, and J. Kemmer, "A multisegment annular Si-detector system for RBS analysis," *Nucl. Instrum. Methods Phys. Res. B* **35**, 522–529 (1988).
- ⁸¹R. P. Gardner and L. Wielopolski, "A generalized method for correcting pulse-height spectra for the peak pileup effect due to double sum pulses," *Nucl. Instrum. Methods Phys. Res. A* **140**, 289–296 (1977).

- ⁸²N. P. Barradas and M. A. Reis, "Accurate calculation of pileup effects in PIXE spectra from first principles," *X-Ray Spectrom.* **35**, 232–237 (2006).
- ⁸³K. Taguchi, E. C. Frey, X. Wang, J. S. Iwanczyk, and W. C. Barber, "An analytical model of the effects of pulse pileup on the energy spectrum recorded by energy resolved photon counting x-ray detectors," *Med. Phys.* **37**, 3957–3969 (2010).
- ⁸⁴K. Taguchi, M. Zhang, E. C. Frey, X. Wang, J. S. Iwanczyk, E. Nygard, N. E. Hartsough, B. M. W. Tsui, and W. C. Barber, "Modeling the performance of a photon counting x-ray detector for CT: Energy response and pulse pileup effects," *Med. Phys.* **38**, 1089–1102 (2011).
- ⁸⁵B. Ohnesorge, T. Flohr, K. Schwarz, J. P. Heiken, and K. T. Bae, "Efficient correction for CT image artifacts caused by objects extending outside the scan field of view," *Med. Phys.* **27**, 39–46 (2000).
- ⁸⁶A. A. Zamyatin and S. Nakanishi, "Extension of the reconstruction field of view and truncation correction using sinogram decomposition," *Med. Phys.* **34**, 1593–1604 (2007).
- ⁸⁷J. Hsieh, E. Chao, J. Thibault, B. Grewowicz, A. Horst, S. McOlash, and T. J. Myers, "A novel reconstruction algorithm to extend the CT scan field-of-view," *Med. Phys.* **31**, 2385–2391 (2004).
- ⁸⁸J. Xu, K. Taguchi, and B. M. W. Tsui, "Statistical projection completion in x-ray CT using consistency conditions," *IEEE Trans. Med. Imaging* **29**, 1528–1540 (2010).
- ⁸⁹T. G. Schmidt and F. Pektas, "Region-of-interest material decomposition from truncated energy-resolved CT," *Med. Phys.* **38**, 5657–5666 (2011).
- ⁹⁰M. Courdurier, F. Noo, M. Defrise, and H. Kudo, "Solving the interior problem of computed tomography using a priori knowledge," *Inverse Probl.* **24**, 065001 (2008).
- ⁹¹H. Kudo, M. Courdurier, F. Noo, and M. Defrise, "Tiny a priori knowledge solves the interior problem in computed tomography," *Phys. Med. Biol.* **53**, 2207–2231 (2008).
- ⁹²H. Yu, Y. Ye, and G. Wang, "Interior reconstruction using the truncated Hilbert transform via singular value decomposition," *J. X-Ray Sci. Technol.* **16**, 243–251 (2008).
- ⁹³G. Wang, H. Yu, and Y. Ye, "A scheme for multisource interior tomography," *Med. Phys.* **36**, 3575–3581 (2009).
- ⁹⁴H. Yu and G. Wang, "Compressed sensing based interior tomography," *Phys. Med. Biol.* **54**, 2791–2805 (2009).
- ⁹⁵H. Yu, J. Yang, M. Jiang, and G. Wang, "Supplemental analysis on compressed sensing based interior tomography," *Phys. Med. Biol.* **54**, N425–N432 (2009).
- ⁹⁶K. Taguchi, J. Xu, S. Srivastava, B. M. W. Tsui, J. Cammin, and Q. Tang, "Interior region-of-interest reconstruction using a small, nearly piecewise constant subregion," *Med. Phys.* **38**, 1307–1312 (2011).
- ⁹⁷P. M. Shikhaliev, "Beam hardening artefacts in computed tomography with photon counting, charge integrating and energy weighting detectors: A simulation study," *Phys. Med. Biol.* **50**, 5813–5827 (2005).
- ⁹⁸T. G. Schmidt, "Optimal 'image-based' weighting for energy-resolved CT," *Med. Phys.* **36**, 3018–3027 (2009).
- ⁹⁹T. G. Schmidt, "CT energy weighting in the presence of scatter and limited energy resolution," *Med. Phys.* **37**, 1056–1067 (2010).
- ¹⁰⁰S. Leng, L. Yu, J. Wang, J. G. Fletcher, C. A. Mistretta, and C. H. McCollough, "Noise reduction in spectral CT: Reducing dose and breaking the trade-off between image noise and energy bin selection," *Med. Phys.* **38**, 4946–4957 (2011).
- ¹⁰¹D. F. Yu and J. A. Fessler, "Mean and variance of single photon counting with deadtime," *Phys. Med. Biol.* **45**, 2043–2056 (2000).
- ¹⁰²D. F. Yu and J. A. Fessler, "Mean and variance of coincidence counting with deadtime," *Nucl. Instrum. Methods Phys. Res. A* **488**, 362–374 (2002).
- ¹⁰³K. Taguchi, S. Srivastava, Q. Tang, B. S. Caffo, J. S. Iwanczyk, N. E. Hartsough, W. C. Barber, and J. Cammin, "Pulse pileup statistics for energy sensitive photon counting detectors with pulse height analysis," in *Medical Imaging 2012: Physics of Medical Imaging*, edited by R. M. N. Norbert J. Pelc and Bruce R. Whiting (SPIE, San Diego, CA, 2012), Vol. 8313, pp. 83130Z-1-7.
- ¹⁰⁴A. S. Wang, D. Harrison, V. Lobastov, and J. E. Tkaczyk, "Pulse pileup statistics for energy discriminating photon counting x-ray detectors," *Med. Phys.* **38**, 4265–4275 (2011).
- ¹⁰⁵P. M. Shikhaliev, T. Xu, and S. Molloy, "Photon counting computed tomography: Concept and initial results," *Med. Phys.* **32**, 427–436 (2005).
- ¹⁰⁶D. P. Cormode, E. Roessl, A. Thrane, T. Skajaa, R. E. Gordon, J.-P. Schlomka, V. Fuster, E. A. Fisher, W. J. M. Mulder, R. Proksa, and Z. A. Fayad, "Atherosclerotic plaque composition: Analysis with multicolor CT and targeted gold nanoparticles," *Radiology* **256**, 774–782 (2010).
- ¹⁰⁷D. Pan, E. Roessl, J.-P. Schlomka, S. D. Caruthers, A. Senpan, M. J. Scott, J. S. Allen, H. Zhang, G. Hu, P. J. Gaffney, E. T. Choi, V. Rasche, S. A. Wickline, R. Proksa, and G. M. Lanza, "Computed tomography in color: NanoK-Enhanced spectral CT molecular imaging," *Angew. Chem., Int. Ed.* **49**, 9635–9639 (2010).
- ¹⁰⁸D. Pan, T. A. Williams, A. Senpan, J. S. Allen, M. J. Scott, P. J. Gaffney, S. A. Wickline, and G. M. Lanza, "Detecting vascular biosignatures with a colloidal, radio-opaque polymeric nanoparticle," *J. Am. Chem. Soc.* **131**, 15522–15527 (2009).
- ¹⁰⁹M. Funaki, Y. Ando, R. Jinnai, A. Tachibana, and R. Ohno, "Development of CdTe detectors in acrorad," (2005) (available URL: http://www.acrorad.co.jp/_skin/pdf/Development_of_CdTe_detectors.pdf).
- ¹¹⁰J. Jakubek, J. Dammer, C. Granja, T. Holy, S. Pospisil, and J. Uher, "Compact system for high resolution x-ray transmission radiography, in-line phase enhanced imaging and micro CT of biological samples," *Nuclear Science Symposium Conference Record (IEEE, San Diego, CA, 2006)*, Vol. 2, pp. 1077–1080.
- ¹¹¹J. Dammer, P. M. Frallicciardi, J. Jakubek, M. Jakubek, S. Pospisil, E. Prenerova, D. Vavrik, L. Volter, F. Weyda, and R. Zemek, "Real-time in-vivo μ -imaging with Medipix2," *Nucl. Instrum. Methods Phys. Res. A* **607**, 205–207 (2009).
- ¹¹²R. Hanus, J. Dammer, T. Holy, J. A. N. Jakubek, S. Pospisil, and R. Tykva, "Small-scale in vivo imaging of soft tissues by radioscopy using single x-ray photon counting," *J. Microsc.* **226**, 191–194 (2007).
- ¹¹³J. Cammin, S. Srivastava, G. S. K. Fung, and K. Taguchi, "Spectral response compensation for photon counting clinical x-ray CT and application to coronary vulnerable plaque detection," in *Proceedings of The Second International Meeting on Image Formation in X-Ray Computed Tomography*, edited by F. Noo, Salt Lake City, UT, 2012, pp. 186–189.
- ¹¹⁴M. S. Polad, "The upper limits of the SNR in radiography and CT with polyenergetic x-rays," *Phys. Med. Biol.* **55**, 5317–5339 (2010).
- ¹¹⁵J. Cammin, S. Srivastava, Q. Tang, W. C. Barber, J. S. Iwanczyk, N. E. Hartsough, and K. Taguchi, "Compensation of nonlinear distortions in photon-counting spectral CT: Deadtime loss, spectral response, and beam hardening effects," *Proc. SPIE* **8315**, 8313–8366 (2012).
- ¹¹⁶S. Kappler, E. Kraft, B. Kreisler, F. Schoeck, and T. G. Flohr, "Imaging performance of a hybrid research prototype CT scanner with small-pixel counting detector," in *Workshop on Medical Applications of Spectroscopic X-ray Detectors* (CERN, Geneva, Switzerland, 2013).
- ¹¹⁷J. Hsieh, R. C. Molthen, C. A. Dawson, and R. H. Johnson, "An iterative approach to the beam hardening correction in cone beam CT," *Med. Phys.* **27**, 23–29 (2000).
- ¹¹⁸A. So, J. Hsieh, J.-Y. Li, and T.-Y. Lee, "Beam hardening correction in CT myocardial perfusion measurement," *Phys. Med. Biol.* **54**, 3031–3050 (2009).
- ¹¹⁹P. Stenner, B. Schmidt, T. Allmendinger, T. Flohr, and M. Kachelrieß, "Dynamic iterative beam hardening correction (DIBHC) in myocardial perfusion imaging using contrast-enhanced computed tomography," *Invest. Radiol.* **45**, 314–323 (2010).
- ¹²⁰Y. Li, V. R. Sheth, G. Liu, and M. D. Pagel, "A self-calibrating PARACEST MRI contrast agent that detects esterase enzyme activity," *Contrast Media Mol. Imaging* **6**, 219–228 (2011).
- ¹²¹F. A. Jaffer and R. Weissleder, "Seeing within: Molecular imaging of the cardiovascular system," *Circ. Res.* **94**, 433–445 (2004).
- ¹²²D. Pan, S. D. Caruthers, G. Hu, A. Senpan, M. J. Scott, P. J. Gaffney, S. A. Wickline, and G. M. Lanza, "Ligand-directed nanobiosensors as therapeutic agent for drug delivery and manganese-based magnetic resonance imaging of vascular targets," *J. Am. Chem. Soc.* **130**, 9186–9187 (2008).
- ¹²³A. H. Schmieder, P. M. Winter, S. D. Caruthers, T. D. Harris, T. A. Williams, J. S. Allen, E. K. Lacy, H. Zhang, M. J. Scott, G. Hu, J. D. Robertson, S. A. Wickline, and G. M. Lanza, "Molecular MR imaging of melanoma angiogenesis with 3-targeted paramagnetic nanoparticles," *Magn. Reson. Med.* **53**, 621–627 (2005).
- ¹²⁴F. Hyafil, J.-C. Cornily, J. E. Feig, R. Gordon, E. Vucic, V. Amirbekian, E. A. Fisher, V. Fuster, L. J. Feldman, and Z. A. Fayad, "Noninvasive detection of macrophages using a nanoparticulate contrast agent for computed tomography," *Nat. Med.* **13**, 636–641 (2007).
- ¹²⁵O. Rabin, J. Manuel Perez, J. Grimm, G. Wojtkiewicz, and R. Weissleder, "An x-ray computed tomography imaging agent based on long-circulating bismuth sulphide nanoparticles," *Nature Mater.* **5**, 118–122 (2006).

- ¹²⁶P. M. Winter, H. P. Shukla, S. D. Caruthers, M. J. Scott, R. W. Fuhrhop, J. D. Robertson, P. J. Gaffney, S. A. Wickline, and G. M. Lanza, "Molecular imaging of human thrombus with computed tomography," *Acad. Radiol.* **12**, S9–S13 (2005).
- ¹²⁷S. A. Anderson, R. K. Rader, W. F. Westlin, C. Null, D. Jackson, G. M. Lanza, S. A. Wickline, and J. J. Kotyk, "Magnetic resonance contrast enhancement of neovasculature with alpha-v beta-3-targeted nanoparticles," *Magn. Reson. Med.* **44**, 433–439 (2000).
- ¹²⁸S. Flacke, S. Fischer, M. J. Scott, R. J. Fuhrhop, J. S. Allen, M. McLean, P. Winter, G. A. Sicard, P. J. Gaffney, S. A. Wickline, and G. M. Lanza, "Novel MRI contrast agent for molecular imaging of fibrin: Implications for detecting vulnerable plaques," *Circulation* **104**, 1280–1285 (2001).
- ¹²⁹P. M. Winter, S. D. Caruthers, A. Kassner, T. D. Harris, L. K. Chinen, J. S. Allen, E. K. Lacy, H. Zhang, J. D. Robertson, S. A. Wickline, and G. M. Lanza, "Molecular imaging of angiogenesis in nascent Vx-2 rabbit tumors using a novel $\{\alpha\}^{\nu}\{\beta\}^3$ -targeted nanoparticle and 1.5 tesla magnetic resonance imaging," *Cancer Res.* **63**, 5838–5843 (2003).
- ¹³⁰P. V. Granton, S. I. Pollmann, N. L. Ford, M. Drangova, and D. W. Holdsworth, "Implementation of dual- and triple-energy cone-beam micro-CT for postreconstruction material decomposition," *Med. Phys.* **35**, 5030–5042 (2008).
- ¹³¹F. Kelcz, P. M. Joseph, and S. K. Hilal, "Noise considerations in dual energy CT scanning," *Med. Phys.* **6**, 418–425 (1979).